UNIVERSIDADE DE LISBOA

FACULDADE DE CIÊNCIAS

DEPARTAMENTO DE FÍSICA

F C Ciências
ULisboa

Thickness characterization of thin Silicon Strip Detectors and its impact in Nuclear Physics Experiments

Francisco Maria Santos Lima Geraldes Barba

Mestrado Integrado Engenharia Física

Dissertação orientada por:
Prof. Dr. Daniel Galaviz
Prof. Dr. Juan Pablo Fernández

2022

Acknowledgments

The beginning of this work was an adventure, and from the moment I was offered this theme onward I must be thankful for the support and patience of my supervisors, Daniel Galaviz and Juan Pablo Fernández. A special thanks for Daniel who offered me the possibility of starting to work with NUC-RIA back in the end of 2017 and helps me ever since not only at an academic level but also as the great man he is. An honorable mention also to Juan Pablo who I know since 2019 and has always been really enthusiastic and allowed me to collaborate with his scientific projects and taught me alot with admirable patience.

The LNS-INFN team must also be thanked. The time I have spent there was very relevant for the understanding of Experimental Nuclear Physics I have nowadays. The team was very receptive and provided me a great environment to learn and express the different questions that arose during my stay there. The visit that led to this work was very much troubled, however, the support of everyone I worked with at LNS allowed me to finish this work and take one more step in the field. A special thanks must be done to Pierpaolo Figuera, Marco LaCognata, Alesia DiPietro, Aurora Tumino, and all the team in BESN experiment.

I must also express my gratitude to all members of NUC-RIA. Every single one has directly or indirectly contributed for this work. From geometric analysis of complex schemes out of scale to singing and whistling orchestras in the office.

My family also had a part on this work. Even though it not visible or countable, it has a lot of care from my parents and good discussions with my siblings that allowed me to better manage time and work.

I am grateful for the many friends who also helped me during this work. However, I would like to highlight two people that were really relevant. My good friend and best "inkeeper" in town, Francisco Proença de Carvalho. He helped me through this time with constant help as a friend and informal advisor. The second person I must thank is Marta Sousa Coutinho, my caring and supporting beloved friend. For keeping track of work, motivation, health (both mentally and physically) and for directly helping with revising and adapting the present work. To them and to all the friends not mentioned, my deepest gratitude.

Regardinf FCUL, I am thankful for the tools and oportunities to grow as a scientist, to understand what academia is and for the support in the projects I have enrolled within the academia.

A.M.D.G.

Resumo

A identificação e precisa caracterização das propriedades de partículas provenientes de reações nucleares é crucial para a compreensão dos mecanismos e interações que governam a física ao nível subatómico. No âmbito desta tese de mestrado, foi determinada a espessura real de detetores de silício segmentados (SSSSD, acrónimo em inglês) no âmbito de uma medida experimental da reação ^{10}Be + ^{120}Sn, realizada no *Laboratorio Nazionale del Sud* (LNS-INFN), em Catânia, no mês de março de 2020. A determinação deste parâmetro permitirá melhorar a capacidade de resolução e extração de informação numa posterior análise dos dados medidos.

Uma partícula é considerada ionizante quando a sua energia é suficiente para excitar ou remover eletrões dos átomos com os quais interage podendo assim quebrar ligações químicas. Estas interações induzem reações no material cujos produtos podem ser convertidos em sinais elétricos que analisados fornecem, direta ou indiretamente, informação sobre a carga, massa e energia da partícula ionizante.

A combinação de diferentes sistemas de deteção fornece em determinadas situações possibilidades de caracterização que sistemas isolados não permitem. Uma dessas combinações é o denominado Telescópio, sistema de deteção composto por dois detetores (um primeiro de espessura fina, e um segundo de maior espessura) situados sequencialmente onde a interação acontece em duas fases. Na primeira fase, a partícula atravessa o detetor depositadando neste uma fração da sua energua chegando à segunda fase onde deposita a restante energia. O poder de paragem de uma partícula carregada num determinado material depende de propriedades da partícula como a sua massa, número atómico ou energia cinética. O sistema telescópio, com a recolha de informação sobre a partícula em duas fases, permite a distinção de diferentes partículas que atingem o detetor com energias cinéticas semelhantes.

As variações de espessura na camada fina do telescópio representam um problema para a identificação das partículas devido à relação entre a energia depositada no primeiro e segundo elementos do sistema de deteção. A caracterização detalhada da espessura do detetor fino possibilitará a correção da energia depositada, resultando numa melhor resolução energética.

O Sistema de deteção utilizado no âmbito da experiência considerada nesta tese foi composto por quatro sistemas Telescópio e dois detetores Monitores. Os sistemas Telescópio foram utilizados para a identificação e medição da energia de partículas provenientes da reação. Para a primeira camada de deteção destes sistemas utilizou-se detetores de silício segmentados verticalmente de um dos lados (SSSSDs), permitindo a discretização do intervalo angular coberto. A camada ativa dos SSSSDs utilizados apresentava uma área de 49.5x49.5 mm^2 e uma espessura de 20 μm, segundo o fabricante. Para a segunda fase de deteção destes telescópios foram utilizados detetores de silício segmentados vertical (no plano dianteiro) e horizontalmente (no plano traseiro), chama-dos de DSSSDs, com uma área ativa de 49.5x49.5 mm^2. A espessura destes detetores, segundo o fabricante, era de 500 μm. Os dois detetores Monitor foram utilizados para a monitorização do feixe e da composição do alvo, consistindo em dois detetores de um único canal de leitura do sinal.
A análise deste trabalho, realizada em sete fases distintas, visava um estudo minuncioso dos

diferentes parâmetros que influenciam o cálculo da espessura atravessada pelas partículas provenientes das reações de calibração e do seu impacto na identificação dos produtos provenientes da reação em estudo na experiência BESN.

A primeira fase foi dedicada à compreensão das motivações por detrás das diferentes configurações utilizadas através do estudo preciso da geometria associada à montagem do sistema de deteção. A identificação de especificidades da montagem (posição, ângulos, distâncias,..), e a análise das trajetórias das partículas a detetar, possibilitou o estudo aprofundado do conceito de coincidências entre os dois detetores dos sistemas Telescópio, constituindo isto a segunda fase do trabalho. Foi nesta fase realizado um estudo de optimização e ajuste, baseado em dados experimentais, da posição e orientação real dos detetores durante a experiência, resultado numa melhor expressão para as fases seguintes.

A terceira fase foi dedicada à calibração energética destes detetores através de uma fonte de partículas α composta por três diferentes núcleos radioativos: ^{239}Pu, ^{241}Am e ^{244}Cm cujos produtos mais prováveis do seu decaimento têm energias compreendidas entre os 5.156 e 5.805 MeV. Ambos os lados do detetor medem os produtos das interações que se formam no interior do detetor, por isso é esperado que as energias medidas por ambos sejam semelhantes. Isso não foi observado na medição de partículas provenientes da reação nuclear para a calibração angular com energias superiores às partículas α. Foi nesta altura realizado um reajuste da calibração escolhendo uma faixa de referência e recalibrando as restantes em relação a esta. O desvio padrão utilizado para a seleção de eventos reduziu, em geral, para metade. Destacou-se o caso em que este valor reduziu de 590 keV para 15.83 keV, ficando próximo dos restantes após os reajustes.

Na quarta fase da análise foi feita a calibração em energia dos SSSSDs. Esta fez uso de uma fonte radioativa de ^{148}Gd, que emite uma partícula α com 3.183 MeV de energia, e de duas reações de ^{10}Be+^{197}Au às energias de 7 e 9 MeV, dado que os productos destas reações depositam toda a energia no detetor fino. Através da consideração do ângulo de entrada e da perda de energia nas camadas não ativas do detetor foi possível estimar a energia com que as partículas chegavam ao material ativo. Comparando os valores nominais, i.e., a energia da partícula α e as energias previstas pelo modelo de dispersão de Rutherford para θ do centro da faixa, com os valores corrigidos pelas considerações mencionadas aprecia-se uma redução de até 8% da energia inicial. Esta redução na energia considerada permitiu uma calibração mais precisa destes detetores, crucial para o cálculo da espessura do material ativo deste detetor.

A determinação da espessura de material ativo dos SSSSDs atravessada por partículas emitidas na direção do pixel do DSSSD onde foram detetadas foi o objetivo da quinta fase da análise. A energia depositada no SSSSD foi medida por produtos da reação utilizada para a calibração emitidas na direção mencionada. Para o cálculo da espessura utilizaram-se dois métodos diferentes. No primeiro, foi considerado que o poder de paragem não aumentava com a perda de energia da partícula no material. Logo, a espessura foi determinada pela relação entre a energia medida e o poder de paragem para ^{10}Be em silício, à energia que este tem antes de atravessar o material. No segundo método foram utilizadas tabelas de alcance de ^{10}Be em silício e, através de uma regressão quadrática, modelou-se a dependência deste parâmetro na energia de partícula incidente. Através deste método a espessura é dada pela diferença entre o alcance da

partícula com energia antes e depois da camada, sendo a espessura posterior dada pela diferença da energia antes da camada e a medida no detetor. A espessura calculada não é a espessura nominal do detetor nessa direção, mas foi obtida por uma correção geométrica e comparada à espessura do fabricante. O segundo método obteve espessuras mais reduzidas quando comparado com o primeiro, dado tomar em consideração o aumento do poder de paragem com a perda de energia no meio. Ambos os métodos apresentaram espessuras nominais que variavam até 35% do valor apresentado pelo fabricante. Apesar da energia depositada no SSSSD corresponder à energia medida para a identificação de partículas, assume-se que a espessura do material ativo é uniforme em todo o detetor. Variações da espessura originam a deposição de energias diferentes por cada fase do detetor por duas partículas iguais com a mesma energia, emitidas em direções distintas.

A sexta fase da análise aplicou correções à energia medida no SSSSD compensando a heterogeneidade da espessura. Inverteram-se os dois métodos de determinação da espessura. O método que utiliza o alcance das partículas num material depende da partícula incidente e da sua energia antes de atravessar o material, impossibilitando a sua utilização. Invertendo o primeiro método de determinação da espessura obteve-se a correção pretendida através do producto da energia medida com a razão entre a espessura média do detetor e a espessura das partículas emitidas na direção de um dado pixel. Foram utilizadas as espessuras obtidas com os dois métodos e comparados os resultados. Em ambos os casos houve uma redução do desvio padrão do pico elástico da reação utilizada para a calibração angular para aproximadamente metade. A correção utilizando as espessuras obtidas a partir do primeiro método obteve valores do desvio padrão até ~17 % inferiores aos do segundo método.

Na última fase da análise, aplicaram-se as correções em espectros de reações de ^{10}Be+^{120}Sn a energias de 31 MeV. Comparando os espectros utilizados para a identificação de partículas antes e depois das correções observa-se um claro aumento da definição das curvas características de cada partícula. É possível distinguir partículas que previamente não eram identificáveis, o que permitirá melhorar a capacidade de resolução e extração de informação numa posterior análise dos dados medidos, cumprindo com sucesso o objetivo do trabalho.

Palavras-chave: Reações nucleares, Instrumentação nuclear, Detetores de silício, Detetores Telescópio

Abstract

The identification and precise characterization of nuclear reaction products is crucial for the study and understanding of the interactions that govern physics at the subatomic level. One of the options developed to discriminate different particles with similar energy is the composition of several stage detectors, usually called Telescope Detection Systems.

In this work four Single Sided Silicon Stripped detectors with thicknesses of ≈ 20 μm have been characterized to improve their response as ΔE in Telescope detection systems. The characterization resulted in the precise determination of the detector thickness throughout its surface. Two different methods were applied to achieve this goal. Maximum deviations of up to 35 % were observed. This charactererization will allow for a better resolution of the system and a clearer discrimination of the reaction products.

Several steps were undertaken during the analysis. The angular calibration of the setup was performed using the scattering reaction ^{10}Be + ^{197}Au at energies below the Coulomb barrier. The energy calibration of the E stage was performed using radioactive sources and corrected for high energies by applying a gain match procedure that allowed a tighter constrain in the event selection. The energy calibration of the thin detectors, done with low energy nuclear reactions and radioactive sources, had to consider the struggling of particles in the dead layers of the material to correctly determine the energy deposited by incident particles in the active detector layer.

The results of this work will allow a more precise analysis of the reaction data on the exotic nucleus ^{10}Be on the magic nucleus ^{120}Sn, measured for the first time at energies around the Coulomb Barrier, at the LNS laboratory in Catania (Italy)

Contents

List of Tables

List of Figures

Acronyms

SSSSD - Single Sided Silicon Strip Detector

DSSSD - Double Sided Silicon Strip Detector

GG - Gate Generator

CPU - Central Processor Unit

FIFO - Fan-in Fan-Out Module

GG - Gate Generator

LNS - Laboratorio Nazionale del Sud

INFN - Instituto Nazionale di Fisica Nucleare

PID - Particle Identification

CMS - Compact Muon Solenoid

LHC - Large Hadron Collider

CERN - *Conseil Européen pour la Recherche Nucléaire*

HE - High Energy

CSP - Charge Sensitive Preamplifier

ADC - Analog Digital Converter

Pr - Projected Range

Chapter 1

Introduction

The detection of particles emitted from nuclear reactions and decays has played a main role in the study of these phenomena. The first detection of particles coming from radioactive isotopes was performed in 1896, by chance, when Henri Becquerel placed some salts he believed were phosphorescent (that is, emit photons when exposed to electromagnetic radiation) over some photographic plates. These were stored in a drawer wrapped in black paper and when Becquerel went to get them found that the photographic plates recorded an image similar to that of the disposition of the uranium salts on the plate [1]. This lead to the first detection of particles coming from nuclear decays. Pierre and Jacques Curie developed a method for detection of very low electrical currents (as low as few pA) [2]. This was the first device measuring the ionization induced by products from radioactive decays. It allowed the detection of the electric field produced in air around the uranium samples. In the proceedings of this work, in 1897 Marie Curie discovered that radium produces a similar response.

Rutherford, in 1899, distinguished the radiation coming from uranium in two types of particles: α-particles, easily absorbed by materials, and β-particles that could better penetrate these [3]. In 1903 William Crookes published his discovery that when a small crystal of phosphorescent zinc sulphide is exposed to radiation from radium it was possible to see little dots of light, when viewed under a microscope [4]. This scintillation method allowed precise counting of emitted particles and was used by Geiger and Marsden in their experiments of scattering alpha particles in different materials. These experiments included the measurement of α-particles back scattered by the foils used and by analysis of the rates at which the particles reached the different regions of the scintillation screen.

The methods of detection of radiation coming from these isotopes kept evolving and in the 1940's particle detectors made of silicon started being deveoped and used for Nuclear Physics experiments. The interest over this material rose due to the low energy needed to produce charge carriers used for the production of a measurable electric signal proportional to the energy deposited in the detector. K.G. McKay published a paper regarding a germanium counter [5] where is measured the response of a crystal of n-type germanium with a point contact with phosphor. Exposed to radiation from radium, this detector revealed a very fast response and a big improvements on the amount of collected charge carriers and its variations when compared with detectors made of different crystals such as diamond. Technology advances in the production of these detectors allowed to create thinner detectors for applications where the

particle would pass through the detector instead of stopping inside it. These detectors were mainly implemented in tracking systems [6], where the track of a particle is obtained from the positions of detectors that the particle crosses, and in Particle Identification (PID) by the use of Telescope detection systems. These consist of two detectors where an incoming particle will interact. On the first detector only a fraction of its energy will be deposited, by having thin detectors, and in the second the remaining energy will be deposit, bringing the particle to rest. By comparing the energy measured in both detectors it is possible to identify particles and measure their total energy before interacting with the detector.

The production of thin silicon detectors at this moment allows the production of stripped detectors, that spatially discretize the readout of signal in the active area, with thicknesses as low as 20 μm [7]. The detectors characterized in the scope of this Master Thesis are thin silicon stripped detectors used as first detector of telescopes. Their thickness characterization produces relevant improvements on the identification of particles coming from a nuclear reaction. The work starts by addressing how particles interact with materials and a view over nuclear reactions. This is followed by a deeper explanation of the working principles of silicon detectors where some examples of application of stripped detectors are explored. Next, a contextualisation is given on the motivations of the experiment in which the detectors to be characterized were used, preceding a more extended analysis over all components of the experiment. All the steps done for the thickness characterization of the thin silicon stripped detectors are presented next in the work. This includes calibration, adjustments, estimation of thicknesses through different methods and finally applying the results to actual experimental spectra. To finish, the conclusions of the work are given.

Chapter 2

Basic Concepts

The information that is obtained from Nuclear Physics experiments has always relied on the detection of particles emitted from nuclear reactions or decays. The understanding of how particles interact with matter is crucial for their detection. Complementary, the study of Nuclear Reactions is one of the most relevant tools to explore the subatomic realm. In this chapter, some relevant aspects related to how ionising particles interact with matter will be presented, as well as some of the important characteristics and concepts from Nuclear Reactions.

2.1 Interaction of Ionising Particles with Matter

A particle is considered an *ionising particle* if its energy is enough to remove electrons from atoms, break chemical bounds and, therefore, interact with matter. At the most fundamental level, in order to detect these, they must undergo some type of interaction with the detector's material. Depending on the type of particle, its properties (mass, charge, kinetic energy) and the kind of material of the detector, different interactions may take place. Most of the time it is not possible to directly detect the emitted particle but only secondary particles emerging from intermediate reactions.

The study of these interactions is not only crucial for the understanding and design of detectors for the different types and energetic regimes of particles, but also for the better understanding of the response of these same detectors when analysing experimental data. This Section gives a look at the various mechanisms that govern the interactions of different types of particles based on the approach given in [8].

2.1.1 Neutral Particles

Regarding particles without electric charge, we can differentiate between photons and neutrons. These two kind of particles, despite the fact of being charge-less, interact very differently with matter.

On one side, photons interact mainly through three types of interaction: Photoelectric absorption, Compton Scattering and Pair Production. The probability of interaction associated to these processes strongly depends on the energy of the incident photon and the characteristics of the absorbing material.

Considering a mono energetic colimated γ-ray beam with intensity I_0 passing through an

absorbing material of thickness x and density ρ, the total intensity of the beam after the material will be given by,

$$I = I_0 e^{(-\frac{\mu_c}{\rho})\rho x}, \tag{2.1}$$

where μ_c represents the *linear attenuation coefficient*, which is the sum of the probability of each interaction for that material and photon energy. The product ρx is called *mass thickness* and is vastly used to describe the thickness of a given material. It is typically given in mg/cm^2.

On the other side, neutrons are more massive than electrons, and therefore only lose energy through interactions with atoms' nuclei in the material. They cannot directly ionize the medium, so their detection implies the production or transfer of energy to particles that are able to induce a response that can later-on be detected. Considering neutrons with energy below 0.5 eV (slow neutrons), these can interact via Elastic Scattering, but due to their low energy are mostly detected by neutron induced reactions, such as (n, p), (n, α) and (n, γ). These reactions must have positive Q-value (further explained in 2.2.1), as the neutrons energy is very small, and most will emit ionising particles that will induce a response that can be measured.

In the case of fast neutrons (with energy greater than 0.5 eV), Elastic Scattering will represent a more significant process, as the energy transferred to the nuclei can produce a detectable recoil product. For very fast neutrons (energies higher than 0.1 MeV) some Inelastic Scattering might happen, where the scattered nucleus will be excited and de-excited by the emission of a γ-ray that can be detected.

2.1.2 Light Charged Particles

On the case of light charged particles, electrons (e^-) and positrons (e^+) will be considered. The main interaction mechanisms of these particles with matter are Elastic and Inelastic Scattering, Bremsstrahlung and Positron Annihilation.

Considering the elastic scattering, it happens mostly based on electromagnetic interaction where the e^- or e^+ interact with atomic electrons that remain mostly unchanged by the interaction. On the other hand, in the case of inelastic scattering the atom can be excited or even ionised, leading to de-excitation and photon emission or even further excitations from the ionized atom.

Bremstrahlung Radiation is emitted due to the deceleration of a charged particle caused by the interaction of the particle with the electric field of the nucleus. That interaction leads to the emission of one or several photons with energies ranging from zero to the energy of the incident particle. It is one of the most important means of energy loss for electrons.

For the case of positrons, that are the anti-particle of the electrons, they usually suffer similar processes as electrons, but in addition can annihilate with an e^-, which will predominantly lead to the emission of two photons of 511 keV emitted in opposite directions.

2.1.3 Heavy Charged Particles

Let us explore the interactions that contribute to the detection of Heavy Charged Particles such as protons, α-particles and heavy ions. These particles mainly interact through Coulomb forces (Elastic and Inelastic Scattering) with both atomic electrons and nuclei present in the medium. In case the particles energy is greater than the Coulomb Barrier between the projectile and the target nucleus it is possible for nuclear reactions to take place.

When a charged particle enters a material it will immediately interact with several atomic electrons, through the Coulomb interaction. The positively charged particle passing by an electron will electromagnetically pull it. This interaction may bring the electron into a higher level within the atomic electronic configuration or even remove this electron from its atom, corresponding these processes to excitation and ionisation, respectively. In the case of ionisation, the ionised electron might have enough energy to further ionise other atoms (see SubSection 2.1.2). Concerning the projectile, it will loose energy up to

$$E_{max} = 4T\frac{m_0}{m} \tag{2.2}$$

in each interaction, where T and m are the kinetic energy and mass of the projectile, and m_0 is the electron's mass [9]. Due to the mass difference between the particles and electrons, the maximum energy loss is very small and therefore, by conservation of linear momentum, the particle suffers little deflection from its initial trajectory. The particle will then have to undergo several interactions in order to loose all its energy and its trajectory inside the material will be rather straight until the point where the particle's energy is close to zero.

2.1.4   Bethe-Bloch Formula

In the previous Section, a merely qualitative description of the various ways through which heavy charged particles lose energy was given. A more quantitative analysis brings the discussion to the concept of Linear Stopping Power defined by the energy loss (E_{dep}) by unit of length (x), thus being given by:

$$S = -\frac{dE_{dep}}{dx} \tag{2.3}$$

for Charged Particles at non-relativistic energies this quantity can be estimated by the Bethe-Bloch approach

$$-\frac{dE}{dx} = \frac{4\pi e^4 z^2}{m_0 v^2}\rho N_a \frac{Z^2}{AM_u}ln\frac{2m_0v^2}{I} \tag{2.4}$$

where N_a is the mass density of the absorbent material, z and v are respectively the charge and velocity of the projectile, ρ, Z and A are the mass density, atomic number and atomic relative mass of the material, e and m_0 are the charge and rest mass of electron and I stands for the average excitation and ionisation energy. As the particles that will be considered in the framework of this thesis are of low energy, there is no need to include relativistic considerations in the Stopping Power calculations.

The Stopping Power of different particles in the same material strongly depends on $1/v^2$ and z^2. The lower the particle's kinetic energy, the larger the time that it will effectively interact with the atomic electron, increasing the interaction probability for ionisation or excitation, and thus the Stopping Power. Also, the higher the z, the greater the Coulomb interaction between electrons and the projectile, with more energy being transferred. Considering different materials, the Stopping Power will depend on their electron density, which is given by the term $\rho N_a \frac{Z^2}{AM_u}$, and on the ionization energy I. If a material has a higher electron density, charged particles will be more likely to interact. In terms of dependence in I, the Stopping Power lowers as I is risen as more energy must be deposited in each interaction.

2.2   Nuclear Reactions

Nuclear reactions are processes between subatomic particles. In this type of reactions, particles collide originating a big variety of outcomes.

A common way to represent a nuclear reaction is

$$a + X \rightarrow Y + b \tag{2.5}$$

where a is the accelerated particle, X is the target nucleus at rest, Y and b are the reaction products where Y is a heavy product, while b is a light emitted nucleus. A shorter way of writing eq (2.5) is $X(a,b)Y$.

Depending on the particles' structure and the energy at which the collision takes place different reactions can happen, from simple nuclear *scattering*, where the reacting particles are the same as the products of the reaction, to particle captures that can originate new nuclei. In the case of elastic scattering, it can be either represented by $X(a,a)X$ or by its equation:

$$a + X \rightarrow a + X \tag{2.6}$$

The inelastic scattering is characterized by a similar reaction to the elastic scattering where either the target or projectile nucleus is excited which is notted by tagging the excited nucleus with * sign. In the case of excitation of the projectile it can be represented by $X(a,a^*)X$ or by the equation:

$$a + X \rightarrow a^* + X \tag{2.7}$$

In the case of excitation of the target nucleus the reaction can either be represented by $X(a,a)X^*$ or by the equation:

$$a + X \rightarrow a + X^* \tag{2.8}$$

Nuclear reactions can induce changes in the amount of nucleons in a nucleus of either reacting particle. To represent these reactions in a generalised form it it relevant to account for at least the atomic number, Z representing the number of protons, and the atomic mass number, A representing the number of nucleons in that nucleus. Transfer reactions are an example where one or two nucleons are transfered between projectile and target. An example of the equation of such reactions can be:

$$n + {}_{Z}^{A}X \rightarrow {}_{Z-1}^{A}X + p \tag{2.9}$$

where n and p represent a neutron and a proton, respectively. Some isotopes present a cluster nuclear structure where one it is possible to distinguish two nuclear identities: the core, C, and the valence, v, structures. A breakup reaction happens when these nucleus collide with other at energies that induce the breakup of this nuclear structure. For a breakup reaction where a presents a cluster structure of $(C + v)$ reacting with a nucleus X its equation is given by:

$$a(C + v) + X \rightarrow C + v + X \tag{2.10}$$

Many different types of reactions can take place and their study is crucial for the understanding of how nuclei interact with each other and ultimately came to be.

2.2.1 Kinematics

The conservation of total energy is one of the conservation laws that nuclear reactions follow. Applied to eq (2.5) results

$$m_X c^2 + T_X + m_a c^2 + T_a = m_Y c^2 + T_Y + m_b c^2 + T_b \tag{2.11}$$

where m_i is the rest mass of particle i, T_i is the kinetic energy of the particle and c the speed of light in vacuum. Regrouping the previous equation brings that

$$m_X c^2 + m_a c^2 - m_Y c^2 - m_b c^2 = T_Y + T_b - T_X - T_a \tag{2.12}$$

where it is seen that the energy difference between the initial and final states is equal to the initial mass energy minus the final mass energy. This amount is called the Q-value and can be positive, negative or zero. In the case of the Q-value being greater than zero, the reaction is exothermic, meaning that nuclear mass or biding energy will be released as kinetic energy of the final products. When $Q < 0$ the reaction is considered endothermic, meaning that initial kinetic energy is converted into mass or binding energy [9].

Another conservation law that must be taken into account is the conservation of linear momentum. Considering the plane defined by the direction of a and the direction of one emitted particle b, the other emitted particle must lay in the same plane to conserve linear momentum. Figure 2.1 shows the basic geometry for this reaction and using the linear momentum conservation comes that

$$\begin{cases} p_a = p_b cos\theta + p_Y cos\xi \\ 0 = p_b sin\theta - p_Y sin\xi \end{cases} \tag{2.13}$$
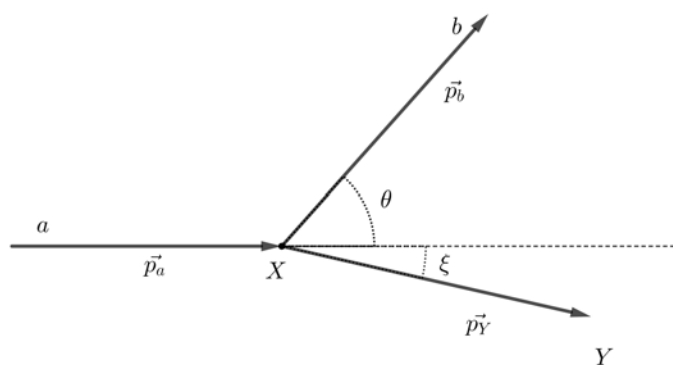
Figure 2.1: Basic geometry of the reaction $a + X \to b + Y$ on the plane defined by the direction of the incident particle and of the reaction products. $\vec{p_i}$ stands for the linear momentum of particle i. Adapted from [9]

Where θ and ξ refer to the polar angles at which the particles are emitted in the defined plane. As most of the times particle Y is a heavy particle that stops in the target, it is useful to get T_b as a function of θ independently of T_Y and ξ. With eq (2.12), eq (2.13) and knowing

the reaction comes that

$$T_b^{1/2} = \frac{(m_a m_b T_a)^{1/2} cos\theta \pm \{m_a m_b T_a cos^2\theta + (m_Y + m_b)[m_Y Q + (m_Y - m_a)]\}^{1/2}}{m_Y + m_b} \qquad (2.14)$$

The T_Y and ξ are possible to calculate through the conservation laws.

Laboratory and Center of Mass Reference Frames Transformations

In experimental Nuclear Physics, all the observations are done in a reference frame at rest in the laboratory, called *laboratory* reference frame. However, in cases where particles have high velocities or due to variable mass difference between the involved nuclei, the observed characteristics may differ from the intrinsic ones. As such, the description in the *center-of-mass* reference frame provides an interpretation of the reaction process, independent of the individual properties (velocity, mass) of the beam and target nuclei.

In this context, it is relevant to establish the relation between the angles in the *laboratory* reference frame, θ, and in the *center-of-mass* reference frame, θ', which is done by taking the Energy Conservation and Linear Momentum Conservation principles. This conversion is fully derived in Appendix C of [10] and shows that:

$$cos\theta = \frac{\gamma + cos\theta'}{\sqrt{1 + \gamma^2 + 2\gamma cos\theta'}} \qquad (2.15)$$

where γ is defined by the ratio of velocities of the center of mass and of particle b in the *center-of-mass* reference frame. When $m_a + m_A \approx m_b + m_B$ the ratio is given by

$$\gamma = \sqrt{\frac{m_a m_b}{m_A m_B} \frac{T_a}{(1 + m_a/m_A)Q + T_a}} \qquad (2.16)$$

In the case of elastic scattering, one gets that $m_a = m_b \wedge m_A = m_B \wedge Q = 0$ simplifying eq (2.16) to

$$\gamma = \frac{m_a}{m_A} \qquad (2.17)$$

Converting angles from the the reference frame of the laboratory to the center of mass is possible with the use of the inverse function

$$cos\theta' = \gamma(cos^2\theta - 1) + cos\theta\sqrt{\gamma^2(cos^2\theta - 1) + 1} \qquad (2.18)$$

2.2.2 Reaction's Cross Section

Depending on the properties of the nuclei involved in a nuclear reaction process, different reactions processes may occur. The probability for a reaction process to happen is given by its cross sections.

Let us consider a beam with N_a particles per unit time t. If the target has N_t target nuclei per unit area and the outgoing particles appear at rate of N_b particles per unit time t, the cross section can be calculated as

$$\sigma = \frac{R_b}{I_a N_t} \quad (2.19)$$

where $R_b = N_b/t$ and $I_a = N_a/t$. Measuring R_b would require a detector measuring all the particles coming from the reaction. Usually detectors only cover a small portion of solid angle, $d\Omega$ (for solid angle, see Section 2.3). The amount of particles emitted from the reaction into this element of solid angle is given by dR_b. Like this, the differential cross section is defined by:

$$\frac{d\sigma}{d\Omega} = \frac{dR_b}{I_a N_t \Delta\Omega} \quad (2.20)$$

where $\Delta\Omega$ is the fraction solid angle covered by the detector.

2.2.3 Rutherford Scattering

Ernest Rutherford was studying the radiation coming from radioactive Uranium and has identified two different types of radiation [3]. One easily absorbed by materials, which he called α-radiation, and another one that could better penetrate in materials, which he called β-radiation. At this time the atomic model was Thompson's model which described the atom as a volume of uniformly distributed positive charge with negative punctual charges (later described as electrons) encrusted on the surface of this volume.

In 1906 Rutherford started studying the interaction of α-particles with matter. The first experiment conducted involved a vessel from where the air could be extracted. He analysed the trajectory of a collimated beam of these particles while passing though vaccum, air or a thin layer of mica, placed after the slit. The particles would then reach a photographic plate where a spot would be produced on the point of collision. This was done under a commuting magnetic field which sign changed every ten minutes over a two hour run. Rutherford observed that the photographic plate showed broader images when the particles passed through materials and stated that "the greater width and lack of definition of the air-lines show evidence of an undoubted scattering of the rays in their passage through air", where the air-lines are the images produced in the plate.

The subject was left aside by Rutherford but Geiger and Ernest Marsden later started a more deep study on the scattering observed, under the surveillance of Rutherford and using a more recent technique, that allowed for the detection and counting of the *alpha*-particles hitting the phosphorescent crystal of Zinc Sulphide under a microscope: the scintillation [11].

In 1908 Geiger conducted a similar experiment observing that the distribution of the α-particles would be within the geometrical image of the slit when the particles would not have to pass through any type of material. However, when the particles would pass through air, a thin foil of gold, or aluminium the area where scintillation was observed greatly increased, overfilling the geometrical image of the slit (see Figure 2.3). Geiger stated that this experiment provided direct evidence of the scattering that these particles undergo when passing through materials could reach appreciable angle. Later in the following year Geiger and Marsden were surprised by observing back scattered particles ($\theta > 90$ °) in a setup built for the purpose of

9

assessing the possibility of measuring scattered alphas at such an angle (see Figure 2.2). The experiment allowed to estimate that the reflections had a rate of about one in eight thousand for their setup and that this rate would increase if the thickness of the reflector material increased [12]. The theory that multiple scattering could be progressively deviating the particle resulting in particles being back scattered was being considered. However, when under experiment, the theory suggested that the probability of an α-particle being deviated by an angle greater than 90° was 8×10^{-40}, which was in disagreement with the previous experiments. Under these evidences the problem was left to Rutherford himself who brought the concept of atomic nucleus to Physics.
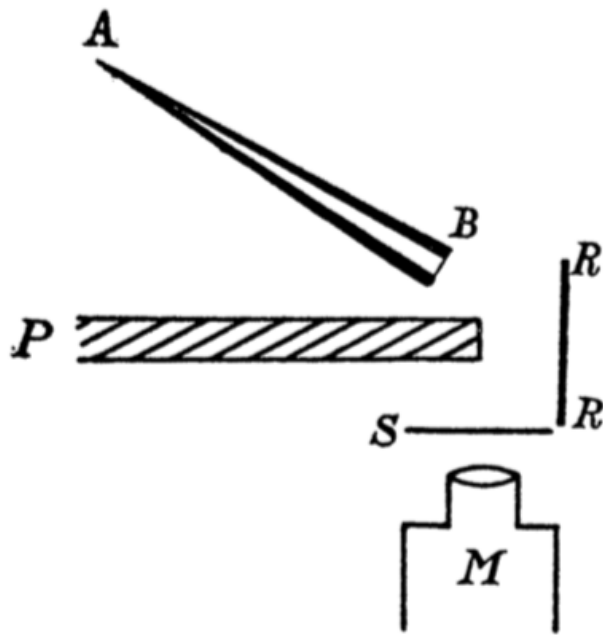
Figure 2.2: Experimental setup used by H. Geiger and E. Marsden in 1909 for the detection of backscattered α-particles. AB is a glass conical tube filled with radium, the end B of the tube is closed airtight by a thin mica foil that allowed the particles to pass through, a zinc sulphide screen is placed in S behind a lead plate P that prevents particles from reaching directly to S. RR is a reflector where the particles would backscatter and M a microscope to allow the counting of scintillations in S [12].

Rutherford suggested that the back scattered particles were due to a single atomic collision. This would only be possible if the α-particle would pass by a very intense electric field. The Thomson's atomic model had the negative electric charges distributed on top of the positively charged bulk. This distribution cancels part of the electric field in the atom making it smaller than the scattering theory needed it to be. Rutherford stated that the atom is composed of a small, centrally located, positively charged nucleus surrounded by a sphere of equal but uniformly distributed negative charge whose effect on the scattering of the particles is negligible. The nucleus would produce an intense electric field that would be able to scatter α-particles at large angles.

This model was tested and confirmed experimentally by Geiger and Marsden in the following years. However, this theory for the atomic structure brought a theoretical problem when

Figure 2.3: Scintillation counts from α-particle interaction with phosphorescent scree as a function of distance from the center of the geometrical ima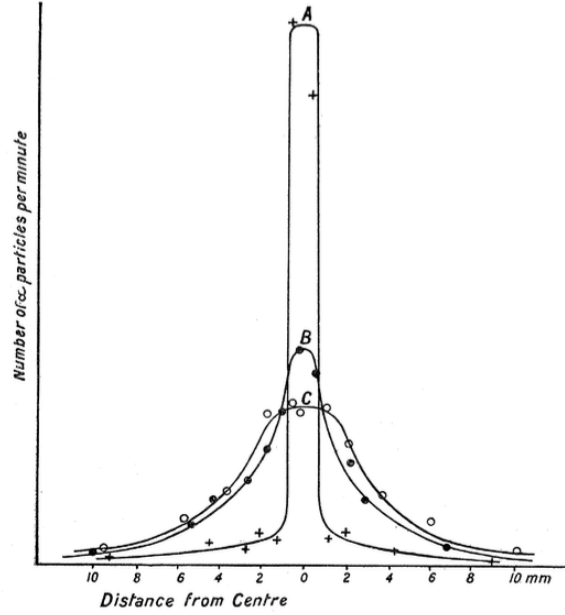ge of the slit through which the particles passed. Cross-points and curve A represent the distribution in charcoal vaccum, filled circles and curve B the distribution when particles pass through a single gold leaf placed after the slit and the unfilled circles and curve C the distribution measured with particles passing through two gold leaves. [13]

analysing the stability of the atom. Rutherford didn't try to address it but in 1913, the same year when Geiger and Marsden published their experimental results in favor of the Rutherford's theory, Bohr succeeded in ensuring stability of the same model, when looking at the problem through a quantum mechanical perspective giving the model general acceptance in the scientific community, opening the door to Nuclear Physics field.

According to this Rutherford's theory, the amount of α-particles scattered per unit area of a ZnS screen placed at an angle θ to the origin direction of the particles and distance d of the scattering point is given by:

$$y = \frac{ntb^2 N_\alpha cosec^4(\theta/2)}{16d^2} \tag{2.21}$$

Where y is the quantity described above, n is the number of atoms per unit volume in the material, t is the thickness and N_α is the total number of α-particles hitting the scattering material. The remaining factor is $b = \frac{2Neq_\alpha}{mu^2}$ where Ne is the charge of the scattering atom, q_α, m and, u are the charge, mass, and initial velocity of the *alpha*-particle. The equation can be read using $T_a = mu^2$ being the kinetic energy of the α-particle bringing that

$$\frac{y}{N_\alpha} = \frac{nt}{d^2}\left(\frac{1}{4T_a}\right)^2 (2Neq_\alpha)^2 \frac{1}{sen^4(\theta'/2)} \tag{2.22}$$

11

In this form is notable the fraction of *alpha*-particles that are scattered to the defined area of the ZnS are proportional to the number of atoms per surface area, and inversely proportional to the distance between the screen, the scattering point, and to the square of the kinetic energy of the *alpha*-particle. The dependence on θ reflects the atomic structure, reducing the probability of the scattered particles for higher angles. Lastly, this quantity is also proportional to the square of the product's charge of the scattered particle and the target nucleus. This last dependence comes from the Coulumb Force, which is the electrical force between the particle and the target nuclei due to their charges given by:

$$F_C = K \frac{Neq_\alpha}{r^2} \tag{2.23}$$

where r is the distance between the particles and the constant is give by $K = \frac{1}{4\pi\epsilon_0}$, with ϵ_0 being the vacuum premittivity.

The differential cross section for this type of scattering looks familiar when compared with equation (2.21) given that it will depend on practically the same parameters, as it would be expected by the definition of the cross section. The expression for this differential cross section is derived using both kinetic and electromagnetic points of view and comes as

$$\frac{d\sigma}{d\Omega} = K(Neq_\alpha)^2 \left(\frac{1}{4T_a}\right)^2 cosec^4 \left(\frac{\theta'}{2}\right) \tag{2.24}$$

This kind of interaction was found not to be restricted to α-particles but applicable to any kind of accelerated charged particle. This was verified through experiments once accelerated nuclear beams became available.

Coulomb Barrier

The Rutherford Scattering is the dominant process at energies lower than the potential barrier created by the electromagnetic interaction, usually called *Coulomb Barrier*. The height of the *Coulomb Barrier* (V_C) is the electrical potential between the two interacting particles when closer as they can get, which is the sum of the radii of those two particles

$$V_C = K \frac{NeE}{(r_\alpha + r_{nuclei})} \tag{2.25}$$

as the radii of the nuclei [9] is easily estimated with

$$r = r_0 A^{\frac{1}{3}} \tag{2.26}$$

where A is the mass number of the nucleus and r_0 is the reduced radius ($r_0 \approx 1.25$ fm).

Reactions at energies around the Coulomb Barrier allow the study nuclear interactions as both elastic and inelastic scattering (the latter due to nuclear reactions with $Q \neq 0$) can be

12
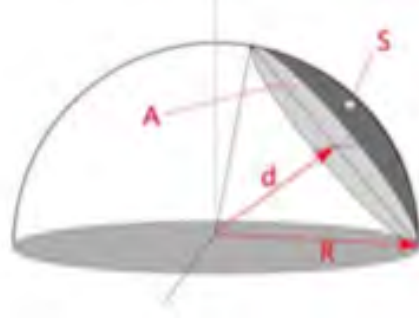
Figure 2.4: A detector with circular active area A at distance d from an isotropic source. S is the projection of A on a sphere with radius R. [14]

compared, allowing the study of nuclear interactions.

2.3 Detector's Solid Angle

The Solid Angle is described as a measure of the field of view covered by a surface S. Its mathematical definition is given by

$$\Omega = \iint\limits_{S} sin(\theta)d\theta d\phi \tag{2.27}$$

where θ and ϕ correspond to the polar and azimutal angles for a coordinate system centered in the source. For an isotropic source the highest value for the solid angle is obtained when the source if fully covered.

$$\Omega = \int_0^{2\pi} \int_0^{\pi} sin(\theta)d\theta d\phi = 2\pi \int_0^{\pi} sin(\theta)d\theta = 4\pi \quad sr$$

It is utmost difficult to have a detector covering a solid angle of 4π str due to practical constraints such as the support needed the detectors, geometrical constraints, or instrumentation access. It is crucial to obtain the solid angle for the detectors when setting an experiment in order to count rates and the coverage that the setup assures.

The solid angle of a detector is extensively analysed in [14] and the following explanation is based on it. The solid angle comes as the angle coverage obtained by the projection of the active area of the detector on a sphere centered in an isotropic source with the smallest radius that encloses the active material, as seen in Figure 2.4.

The surface of a spherical volume is given by

$$S = \Omega R^2 \tag{2.28}$$

13

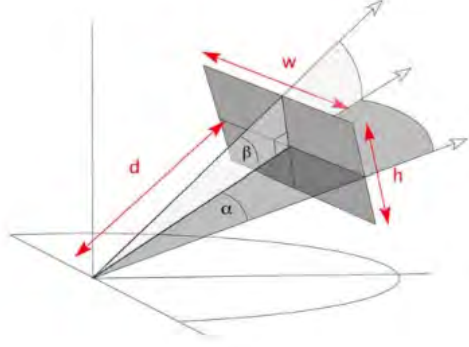Figure 2.5: Geometry of a rectangular detector. I this figure, d stands for the distance of the center of the detector to the source, w to the width of the detector, h to the height of the detector, α and β to the horizontal and vertical angular half-apertures of the detector in this configuration. From [14]

Which for the total surface area of the sphere gives $S_\circ = 4\pi R^2$. The question then relies on the calculation of S. A common approach is to use S as the active area of the detector. That is a good approximation for a detector sitting perpendicularly to the radial direction from the source at a large distance of the detector to the target and small active areas. It is relevant to get the correct solid angle and when the detector is not perpendicular to the radial direction the approximation given is not valid and the accurate calculation of S is necessary.

When considering rectangular detectors perpendicular to the radial direction from the source, the calculation of S comes from measuring the horizontal and vertical aperture of the detector (in the detectors reference frame) in the considered geometry. The solid angle of such a detector can be obtained using:

$$\Omega = (1 - f_s) \cdot 4 \cdot arcsin\left[sin(\alpha) \cdot sin(\beta)\right] \tag{2.29}$$

where f_s is a factor that takes into account eventual shadow made from the detectors frame ad structural components of the system. If there are no such elements $f_s = 0$. The terms α and β are the horizontal and vertical half-apertures as seen in Figure 2.5.

In (2.29) the factor 4 is accounting that the horizontal half-aperture is the same in both halves of the detector (same applies for the vertical aperture). If the detector is somehow tilted, the half horizontal and vertical aperture angles are not symmetric in the different quadrants of the detector. In Figure 2.6 an example of a detector in a different orientation is shown. This leads for a modification on (2.29) turning it into:

$$\Omega = (1 - f_s) \cdot \left\{ arcsin\left[sin(\alpha^+) \cdot sin(\beta^+)\right] + arcsin\left[sin(\alpha^-) \cdot sin(\beta^-)\right] + arcsin\left[sin(\alpha^+) \cdot sin(\beta^-)\right] + arcsin\left[sin(\alpha^-) \cdot sin(\beta^+)\right] \right\}$$
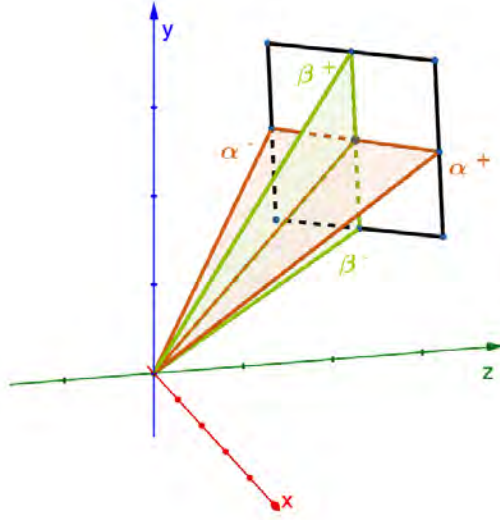
$$\tag{2.30}$$

Figure 2.6: Rectangular detector not perpendicular to the radial direction from the source. The α^+ and α^- refer to the horizontal angular apertures in the detectors reference frame and β^+ and β^- to the vertical ones.

The angular apertures α^+, α^-, β^+ and β^- are as described in Figure 2.6.

Transformation between Laboratory and Center of Mass Reference Frames

As discussed in Section 2.2.1, conversions between laboratory and center of mass reference frames are necessary when willing to compare calculations at the reaction rest frame with observations. The conversion of solid angles from one these reference frames to the other is also analysed in Appendix C of [10]. The differential cross section accounts for the number of reaction products that are emitted to an element of solid angle at a certain direction. These quantities must be the same in any reference frame and for a cross section only dependent on the polar angle of emission comes that:

$$\left(\frac{d\sigma}{d\Omega}\right)_\theta d\Omega = \left(\frac{d\sigma}{d\Omega}\right)'_{\theta'} d\Omega' \tag{2.31}$$

In order to get a factor to use to convert between reference frames:

$$\frac{d\Omega}{d\Omega'} = \frac{(d\sigma/d\Omega)'_{\theta'}}{(d\sigma/d\Omega_\theta)} = \frac{d(cos\theta)}{d(cos\theta')} \tag{2.32}$$

From equation (2.15) it is possible to derive that:

$$\frac{d\Omega}{d\Omega'} = \frac{1 + \gamma cos\theta'}{(1 + \gamma^2 + 2\gamma cos\theta')^{3/2}} = \frac{\sqrt{1 - \gamma^2 sin^2\theta}}{(\gamma cos\theta + \sqrt{1 - \gamma^2 sin^2\theta})^2} \tag{2.33}$$

Getting a factor that is only dependent in one reference system and allows to convert solid angles from one to the other.

Chapter 3

Silicon Detectors

The previous chapter has explained how different particles interact with matter. However, the challenge of detection resides on developing systems that can register these interactions. Along with the passage of a particle through the system, an electronic signal must be generated. Depending on the purpose of the detection that signal might carry information regarding the particle's energy, momentum, charge or even just flag its passage through the detector. Silicon's vast use in industry allowed for a tremendous evolution of detectors based on this semiconductor material. Combined with its own properties, Silicon Detectors are used in a big variety of applications. In digital cameras Silicon is used to detect visible light and produce images [15], in Astrophysics these detectors are used to detect a broad range of wavelengths [16], in Nuclear and Particle Physics these are used to detect ionising particles [17] and in many other areas of science and technology. In Particle Physics specifically, these detectors represent one of the best options in terms of Energy Resolution and Position Determination.

This chapter provides an overview over the main characteristics of semiconductors and the use of these materials as particle detectors, with special focus on silicon detectors. Some examples of experiments that use this technology are also presented for a better understanding of its practical utility.

3.1   General Semiconductor Properties

The electrons from an isolated atom have discrete energy levels. From a Solid State Physics point of view, a lattice of interconnected atoms merges the atomic energy levels into energy bands. There are different energy bands that can be populated by electrons. For an atom in the ground state, the last bounded electrons are in the valence band. Thes e are the easiest electrons to detach from the atomic bond and they also interact with the valence electrons from the neighbouring atoms. This last property makes some of these electrons free to move in the material and therefore unsigned to any atom specifically but to the material itself bringing the concept of Valence Band.

The conductive band is where the electrons move more freely in the material and is separated of the valence band by an energy gap (E_{gap}). Depending on the width of the gap, materials will be classified as conductors, semiconductors or insulators (the different possibilities are presented
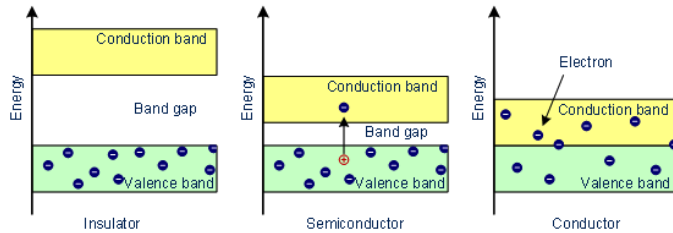
Figure 3.1: Representation of Band Model for different types of materials. On the left, insulators, in the middle semiconductors and on the right conductors.

schematically in Figure 3.1).

In semiconductors this gap is small enough to allow electrons to easily bounce from the valence to the conduction band, but large enough so that electrons stay mainly in the valence band unless they are excited. When an electron is excited into the conductive band, it leaves a hole (h^+) in the valence band that can recombine with another electron migrating in the material. The holes can then be considered positive charge carriers (located in the valence band) and the electrons in the conduction band negative charge carriers. At room temperature, some electrons populate the conductive band and this number increases if the electrons are excited by some energy deposition or higher temperature of the material. The probability per unit time that an electron-hole pair is thermally generated, ρ is given by:

$$p(T) = CT^{3/2}e^{\frac{E_g}{2kT}} \tag{3.1}$$

where T is the absolute Temperature, k is the Boltzman constant, and C is the proportionality constant characteristic of the material [8]. It is possible to see that if the temperature increases, the probability of formation of an electron-hole pair increases. This probability is also highly dependent on the ratio $E_g/2kT$. As the semiconductors present a low E_G ($\sim$few eV), its conductivity is low and increases with the temperature. (Note that for conductors the E_g is zero, therefore the electrons can easily populate the conduction band for these materials and thus resulting in a high conductivity.) Even though the formation of electron-pairs is constantly happening, the material itself remains electrically neutral as the carriers remain disperse in the material.

An intrinsic semiconductor is a material where the amount positive charge carriers per unit value, p, is equal to the amount of negative charge carriers per unit value, n. In an intrinsic material the index i is added to the symbol representing the carriers' concentration to state that the material fulfils the intrinsic condition. For an intrinsic semiconductor, the equilibrium established by the thermal excitation of electrons from the valence to conduction band and their subsequent recombination with holes leads to equal numbers of electrons and holes, bringing that $n_i = p_i$.

When an electric potential is applied to the semiconductor, instead of recombining, the carriers drift parallel to the direction of the electric field. The electrons in the conductive band flow through the material, unbounded to any atom, whereas the holes move by electrons that are pushed into the vacancy recombining with it and leaving a hole in the structure they previously belonged to. These different drift processes in the material result in electrons drifting with higher mobility than the holes. Under small electric fields ($<10^3$ V/cm) and at room temperature, the
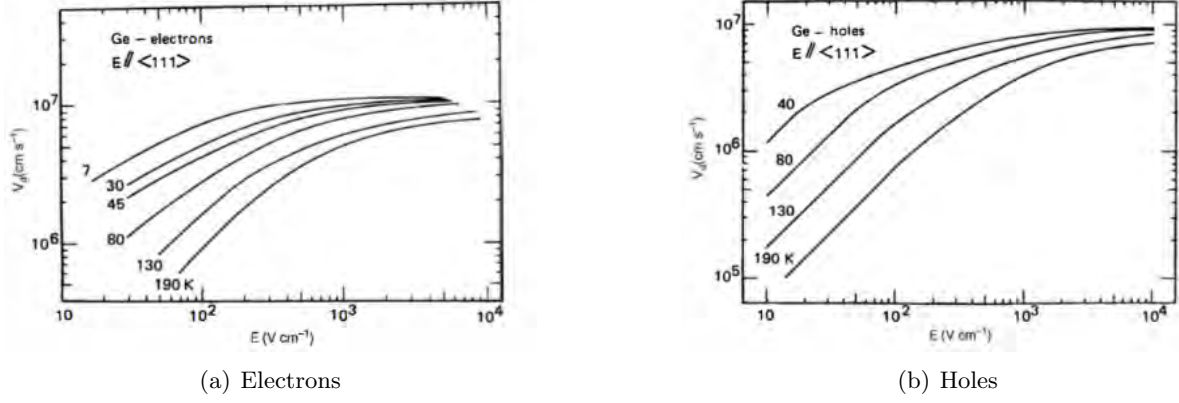
(a) Electrons

(b) Holes

Figure 3.2: Drift velocity of electrons and holes in Si as a function of the applied electric field for different temperatures. [8]

carriers mobility (μ) is approximately constant and the drift velocity of the carriers can be described as:

$$v_h = \mu_h \mathcal{E} \tag{3.2}$$

$$v_e = \mu \mathcal{E} \tag{3.3}$$

where $\mathcal{E}$ is the magnitude of the electric field. For $\mathcal{E}$ between 10^3-10^4 V/cm the mobility varies approximately as $\mathcal{E}^{-1/2}$ and for higher electric fields it follows $1/\mathcal{E}$. For temperatures from 100 K to 400K the mobility varies as T^{-m}, where m is characteristic of the material and on the charge carrier. At higher $\mathcal{E}$ the velocity of the carriers increases slower, eventually getting up to a value above which the velocity does not increase anymore, which is called *saturation velocity*. This behaviour for the mobility and its effect on the drift velocity is seen in Figure 3.2, where the drift velocity is represented as a function of the electric field applied to the semiconductor for different temperatures.

Doped Semiconductors

In intrinsic semiconductors, the amount of holes and electrons on the conduction band is the same. In a Si crystal, each atom uses its four valence electrons to establish four covalent bonds with the closest neighbouring atoms. By adding small amounts of impurities it is possible to change the materials electronic properties.

When an impurity with five valence electrons occupies a substitutional position in a Si crystal it will make four bonds with the neighbour Si atoms, filling the valence band and leaving an unbounded electron (see Figure 3.3(a)). This fifth electron will occupy an energy level slightly below the conduction band, called donor level (see 3.3(b)) and is localised only in the vicinity of such impurities. At room temperature most of the electrons in the donor level will be excited into the conduction band due to the small energy difference between the donor level and the conduction band. This type of material where the main charge carriers are negative is called n-type semiconductor. Note that the excited electrons do not leave a hole in the Valence band as they were not occupying that energy band.

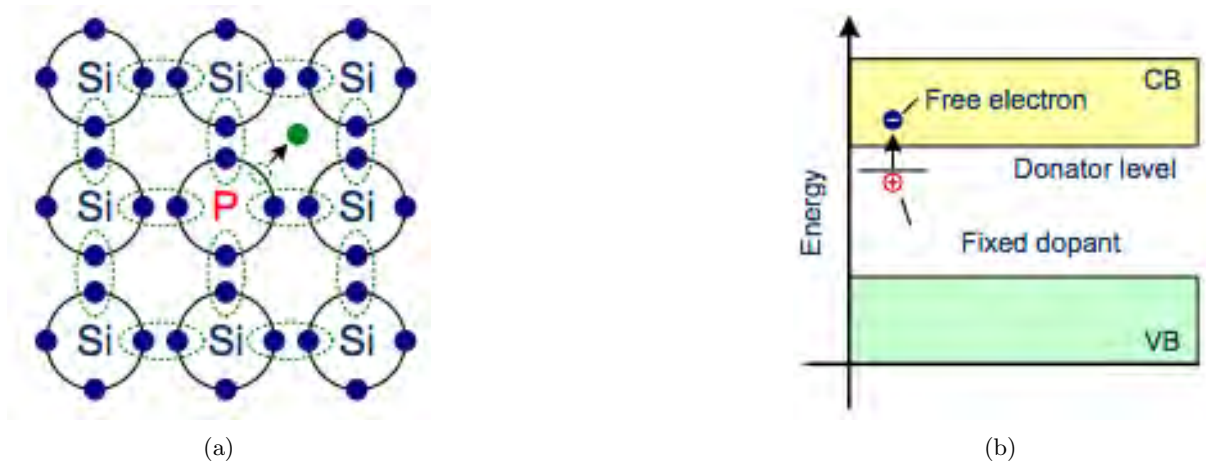For the case of an impurity with three valence electrons occupying a subsitutional position

(a)   (b)

Figure 3.3: (a) Bi-dimensional schematic of Pentavalent impurity (Phosphorus) in substitutional position in Si crystal. (b) Energy Band model for n-type semiconductor where CB is the Conduction Band, VB the Valence Band. [18]

(a)   (b)
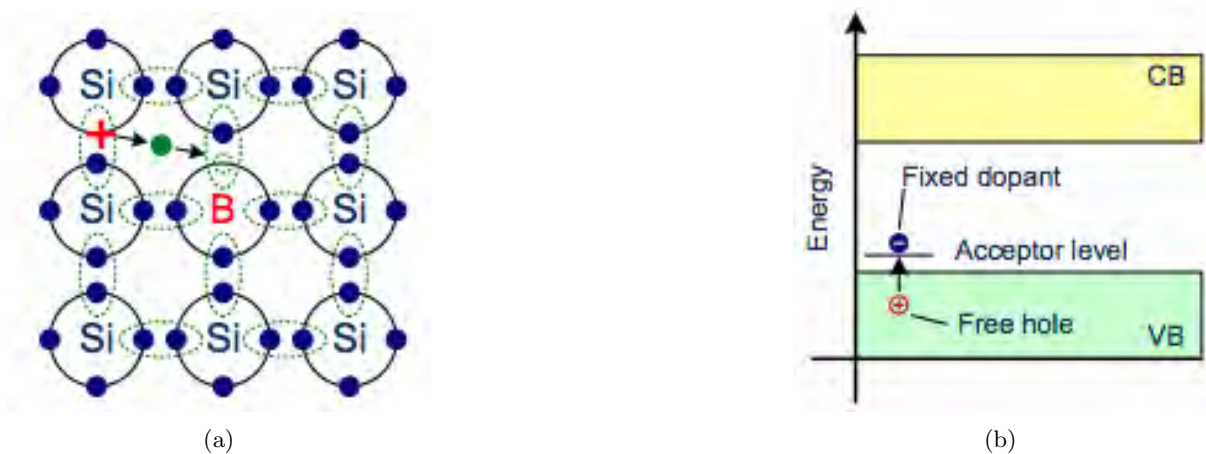
Figure 3.4: (a) Bi-dimensional schematic of Trivalent impurity (Boron) in substitutional position in Si crystal. (b) Energy Band model for p-type semiconductor where CB is the Conduction Band, VB the Valence Band. [18]

in a Si crystal will establish three covalent bonds with its neighbouring Si atoms. As previously stated, the Si atoms establish four covalent bonds with their neighbours but the trivalent impurity lacks one electron to make the fourth bond, leaving a vacancy in the Valence Band. This vacancy is similar to a hole that is originated when a valence electron is excited, but its energy characteristics are slightly different. If a valence electron from a nearby atom is captured to fill this vacancy, it will create a hole and participate in a new covalent bond that is different from the other bonds in the crystal due to the trivalency of the atom (see Figure 3.4(a)). The captured electron will be slightly less firmly attached to the atom than a typical valence electron. This brings the captured electron to an energy level slightly above the valance band, creating a new level within the energy gap, the acceptor level, as seen in Figure 3.4(b). The small energy difference between the acceptor level and the valence band makes that, at room temperature, thermal excitation provides allows electrons to fill the vacancy in the acceptor level, making holes the main charge carrier on this material, making it a p-type semiconductor.

Semiconductors such as Si and Ge crystals have a desity in the order of 10^{22} atoms/cm^3. The usual concentration for impurities in doped materials is in the order of 10^{13} to 10^{18} atoms/cm^3. If the impurities concentration reach 10^{20} atoms/cm^3 the material is considered heavily doped and a + sign is added after the material type (n^+-type and p^+-type semiconductor). Heavily doped semiconductors are often used in making electrical contacts with semiconductor devices.

Semiconductor Junction

A semiconductor radiation detector uses the physical properties that come from the junction of n-type with p-type semiconductors. To get this type of junctions instead of bringing two different types of semiconductor crystals together, the same crystal must be doped with the two different types of impurities.

The two most common processes are Diffusion and Ion Implantation. The first one consists of exposing the Si crystal to a high concentrations of dopant. These impurities will flow through the material due to the concentration gradient, resulting in a gradually mixing of impurities in the crystal. Ion Implantation consists on exposing the surface of the crystal to an accelerated ion beam of impurities that will be stopped/ implanted within the material. The energy of the beam, dopant and substrate material determine the average penetration depth.

Neither of these methods will produce an homogeneously doping in the induced side, due to the physics associated with these methods. However, in order to understand the phenomena that happens in these materials with opposite types of dopants, it will be assumed that the crystal presents a uniform distribution of impurities and is divided in a region of p-type material and another of n-type material, as seen on the left picture of Figure 3.5.

The concentration differences of donor and acceptor impurities along the material forces charge carriers to diffuse, flowing from the regions of higher to lower concentration. This will bring together electrons on the conduction bad and holes in the valence band, inducing holes to capture electrons. Without this recombination, both sides of the material were electrically neutral. Recombination brings that the p-type material will become negatively charged (as the hole on the valence band from the trivalent impurity will be filled by an electron) and the n-type material will become positively charged (as the extra electrons from the pentavalent impurities will combine with the holes). On the right side of Figure 3.5 a schematic representation of the electrical charge distribution after recombination is shown. The region of charge unbalance is called depletion region.
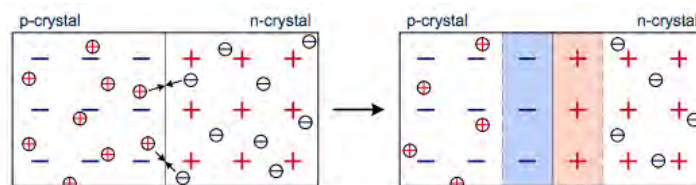
Figure 3.5: On the left a representation of an uniformly doped pn junction without considering the diffusion of free charge carriers. On the right, a representation of a pn junction considering the creation of the depletion zone by the exchange of charge carriers in the junction

The differently charged regions of the crystal create an electric field that will be contrary to the diffusion of charge carriers discussed. There will then be an equilibrium between the created electric field and the amount of charge carriers that flowed to the other type of material

within the crystal. The value for the electrical potential V at any point can be obtained by the Poisson's equation, which in one dimension comes as:

$$\frac{d^2V}{dx^2} = -\frac{\rho(x)}{\epsilon}$$ (3.4)

where ϵ is the dielectric constant of the material, and $\rho(x)$ is the charge distribution, that in the case of being uniformly distributed is given by

$$\rho(x) = \begin{cases} eN_D & 0 < x < x_n \\ -eN_A & -x_p < x < 0 \end{cases}$$ (3.5)

where N_D and N_A are the concentrations of donor and acceptor impurities, x_n and x_d are the depth of the depletion region into the n-type and p-type regions of the junction. The reference axis is centered in the interface and the p-type material is to the left of it. Due to charge conservation also comes that:

$$N_A x_p = N_D x_n$$ (3.6)

As it can be seen, the lower the concentration of a dopant type, the further will it extend the depletion zone into that region. With equations (3.4) and (3.5) it is possible to derive the depth of the depletion given by

$$d = \left(\frac{2\epsilon V_0}{e} \frac{(N_A + N_D)}{N_A N_D} \right)^{1/2}$$ (3.7)

where V_0 is the contact potential (the electric potential difference between the two ends of the depletion zone).

In the depletion zone, the only significantly abundant charges are the immobilized ionized donor sites and filled acceptor sites. These charges do not contribute for conductivity giving the depletion zone a high resistivity when compared with the n- or p- type material outside the depletion zone. The e^-/h^+ pairs created within this region will move along the electric field and generate an electric signal. These pairs can be created by either the passage of radiation or thermal excitation. The generated charges only drift in the region within the depletion region, as it is where the electric field exists. Placing electrodes in the ends of the pn-junction allows the reading of the current provoked by the movement of these charges as from the Schockley-Ramo Theorem [19] comes that the movement of the charges makes changes in the electrostatic flux lines in the electrodes, inducing current in those.

Increasing the depletion region increases the sensitive area of the detector. If potential difference is applied to the terminals of the junction, the free charge carriers will be forced to move and the configuration of the depletion region will change. If negative voltage is applied to the p-side and positive voltage to the n-side (reversed bias voltage), the holes on the p-side will be pulled to the electrode of that side leaving the electrons in the acceptor impurities closer to the formed depletion region. On the n-side the free electrons are pulled to the electrode leaving the atoms closer to the junction positively charged. The width of the depletion region is therefore increased when reverse bias is applied and can be calculated using (3.7), replacing V_0 with $V_0 + V_B$ where V_B is the bias voltage. It is possible to attain full depletion of the junction

21

when enough bias voltage is applied to deplet the full width of the junction. The intensification of the electric field in the junction due to the increase of Reversed Bias Voltage will also increase the energy of the drifted charge carriers produced when the material is excited, contributing for better charge collection and therefore a more sensitive device. The increase in the velocity of drifted charge carriers will allow faster charge collection improving the time properties of the pulse. It is still important to note that increasing the reverse bias will eventually reach breakdown. At this point allowing for intense reverse current. This breakdown happens due to electrons reaching energies capable of creating e^-/h^+ pairs that accelerated by the electric field will do the same creating therefore the large reverse current [20].

3.2   Silicon Detectors

The characteristics analysed on the previous Section make semiconductors good candidates for radiation detectors. Silicon is one of the most used semiconductors for particle detection in Nuclear Physics. When radiation passes through silicon, the energy deposition leads to the creation of e^-/h^+ pairs. The required energy for the creation of a pair (I_0) is typically about 3.6 eV where 1.12 eV correspond to the E_{gap} and the remaining energy is used to induce vibrational excitation of the lattice. The amount of charge carriers produced will then depend on the amount of energy that is deposited in the crystal.

The creation of these pairs is assumed to follows a Poisson distribution corrected by the Fano Factor (F) [8]. For the Poisson distribution it is assumed that the analysed events (in this case, the production of each pair) are independent and that each happens at a mean energy deposition of 3.5 eV. The Fano Factor is a correction to this independence among events that is characteristic of the material and is given by the ratio between the observed variance and the Poisson Predicted Variance. Joining the Poisson distribution with the Fano Factor comes that for N produced pairs, the standard deviation is expected to be $\sqrt{FN}$. The accuracy with which a detector can distinguish between two close peaks measured by its Energy Resolution, R. This parameter is usually given in terms of the Full Width Half Maximum

$$FWHM = 2\sqrt{2ln2}\ \sigma \approx 2.355\sigma \tag{3.8}$$

where σ is the standard deviation of the spectra's peak being analysed. For a calibrated spectra, the energy resolution is give by

$$R = \frac{FWHM}{E_{dep}} \tag{3.9}$$

where E_{dep} is the mean energy deposited on the events of the peak. The measured deposited energy in a detector is proportional to the number of $e-/h^+$ pairs generated which leads to

$$R = 2.355\frac{\sqrt{FN}}{N} = 2.355\sqrt{\frac{FI_0}{E_{dep}}} \tag{3.10}$$

The silicon low I_0 strongly contributes for the good energy resolution of these detectors, when comparing with other alternatives, such as ionisation chambers (with $I_0 \sim 15$ eV). The

Energy Resolution is usually calculated using (3.9) and is given in percentage.

Electrical Contacts

Applying bias voltage to pn-junctions and collecting the charges produced by radiation passage is done by electrodes fitted to both sides of the junctions. However, due to the band structure of conductors, when the metal is put to contact with semiconductor the band structure of the material in the contact region may be altered originating a depletion region that extends into the semiconductor side of the contact forming a so called rectifying junction. These junctions have a broad use in electronics. For the use case of particle detection, it is relevant to keep the *leakage current* as low as possible. This current flows along the electric field applied to the junction transporting both free charge carriers and thermally generated electron-hole pairs, producing a measurable signal. This current will provide noise to the signal detection and prevent the detection of low energy signals.

For preventing this, the contact is made by placing a layer of heavily doped semiconductor between the active material and the electrode. Due to the high doping of this extra layer, the depletion zone that is created due to the electrode is negligible, which can be seen by (3.6).

3.2.1 Silicon Stripped Detectors

Besides its good energy resolution, it is also possible to achieve very good spatial resolution with Silicon Detectors. This kind of stripped detectors is produced by combining photolitography and ion implantation. These two techniques, initially used for integrated circuits fabrication, allow to obtain a spatially resolved detector with very low leakage current. The production of such detectors starts with a polished and clean slightly n-type silicon wafer where an Oxide layer is produced that will improve the leakage current conditions of the final detector. With photolitography selected areas of the oxide are removed and the exposed bulk material is then exposed to p-type impurities on one side and to n-type impurities on the opposite side. These heavily dopped regions will be use both as part of the junction and for the ohmic electrical contacts. For the electrode contacts, Al is evaporated and patterned in the desired geometry. These layers that are not depleted (therefore not in the active region of the material) constitute dead layers through which the particles may pass through, depositing energy that will not be measured by the detector, therefore have to be taken into account when analysing data from the experiment.

Depending on the geometry applied with photolitography these detectors can present different architectures. In this work two different detector architectures were used: the Single Sided Silicon Strip Detector (SSSSD) and the Double Sided Silicon Strip Detector (DSSSD). The concept of these detectors is to subdivide the electrode into independent strips or sections. As the charge carriers produced by the passage of radiation drift along the the electric field lines, these will be led to the closest electrode on each side of the detector, collecting a strong signal only in the strips that measured a relevant amount of charge. These architectures main difference is that the first only have one side with the stripped configuration, allowing for spatial resolution in one

direction, whereas the second has the stripped configuration in both sides where the direction on one side is orthogonal to the direction of the other, allowing for spatial resolution in two directions which leads to the definition of pixels. The two mentioned architectures can be seen in Figure 3.6.

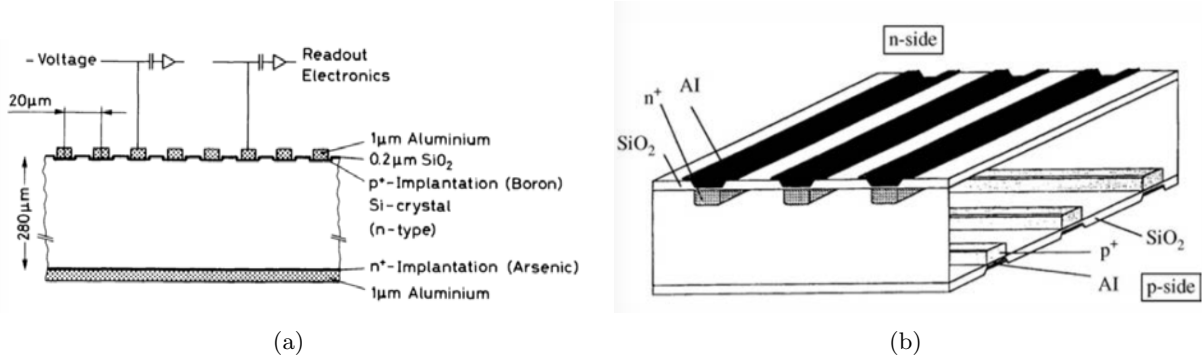(a)   (b)

Figure 3.6: On the left a representation of a SSSSD [21] and on the right a representation example of a DSSSD [8]. Both representations show the different layers of material. The electronics shown on picture on the right is part of the bias voltage supply and readout system.

The strip width defines the spatial resolution of the detector. This spacing can be in the order of a few mm and allow for a precise measurement of the position where the particles passed through. This is rather important when precise angular distributions are to be measured. In this kind of detectors, the interstrip width is usually 0.1 mm in such detectors.

The production of Silicon thin foils has allowed the design of Silicon Thin Detectors with thicknesses that go down tens of μm with surface areas up to 25 cm^2. This layer's aim is not stop the passing particles but only to deposit a small amount of energy in the material. Thin SSSSD are great candidates for the first phase of a Telescope Detector, a commonly used architecture for PID. The use of the stripped detectors allows both the measurement of the energy deposited by the incident particle as well as the position where the particle crossed the detector, resulting in good position and angle tracking properties of the system. The energy deposited on the thin detector is dependent on the length the particle crosses in this stage (see subsection 2.1.4). Homogeneity in the thickness of such detectors is of most importance for a good analysis of the acquired data [22] which can not always be assured when the thickness of the detector comes down to the tens of μm.

3.2.2 Applications of Silicon Stripped Detectors

The characteristics of these detectors discussed above make them an important constituent of different experimental setups.

One of these examples is the Compact Muon Solenoid (CMS), a detector built at the Large Hadron Collider (LHC) in CERN [23]. At the LHC proton beams collide at energies of 14 TeV in the center of mass reference frame with luminosity reaching 10^{34} cm^{-2} s^{-1}. The radiation conditions are very severe in terms of the flux of particles coming from the reactions. The CMS aims to identify the products from the proton reactions by tracking the particles and measuring

their energies. For the tracking process, one of the most powerful magnets ever built is used to bend the track of charged particles while these cross a Silicon Tracker. This phase is in the CMS Inner Tracker and the closest detectors to the collision point are silicon pixel detectors while in the outer layers of the tracker are used SSSSDs with thicknesses ranging from 320 - 500 μm. These detectors were chosen due to their fast response (needed for such intense experiments) and good spatial resolution. The radiation hardness of the material was also a very important as the damage of radiation was known to play a key role. To prevent increased leakege current dur to radiation damage ad annealing of the silicon, the detectors are kept at a temperature of -10 °C.

The GLObal ReactIon Array (GLORIA) is a detector designed to study direct reactions induced by exotic nuclei at energies close to the Coulomb barrier. This arraay consists of six telescopes arranged in close geometry that allows the measurement of reaction fragments in a continuous angular range from 15° to 165° [24]. Silicon detectors were chosen for the stages of the telescope as these have a high detection efficiency for heavy ions at moderate rates (around few kHz/cm^2) and can be designed in DSSSD architecture, allowing for a good spatial resolution. The first and second stage of the telescopes were 40 μm and 1 mm thick DSSSD, respectively. Each DSSSD 16 vertical and 16 horizontal strips with an inter-strip pitch of 100 μm and a total active area of 49.5x49.5 mm^2. The independent DSSSD energy resolution was found to be about 0.5% for the detection of ^{8}He at about 18 MeV. The detector system was shown to successfully distinguish different Helium isotopes by an accurate measurement of the energy and angular distribution of the fragments [24].

Chapter 4

BESN Experiment

BESN is the acronym of an experiment performed in March 2019 at the *Laboratori Nazionale del Sud* (LNS-INFN), in Catania, Italy. The spokespersons of the experiment were J. P. Fernández-García (co-supervisor of this work) and M. A. G. Alvarez, both from the University of Seville (Spain). In the framework of an international collaboration, they proposed the "Study of ^{10}Be+^{120}Sn reaction dynamics at energies around the Coulomb barrier".

This chapter aims at addressing the experimental main motivations, how the radioactive Beryllium beam is produced, the characteristics of the targets used and finally the detectors used in the reaction chamber, giving the reader a whole look into the experiment.

4.1   Experimental Motivation

The study of the properties of nuclear collisions using halo nuclei as probe has been a topic of research over the last decade [25]. Examples of these nuclear systems with one or two weakly bounded nucleons (mainly neutrons) are ^{8}B, ^{11}Li, ^{11}Be and ^{15}C. These studies allow for better understanding of the structure of these nuclei. However, because of their radioactive character, beams of such isotopes have usually low intensities which constrain the experimental execution.

Light weakly bound nuclei beams are available in higher intensities than the halo nuclei and the low breakup threshold with a marked cluster structure allow the study of similar scattering reactions helping to understand the dynamics of halo nuclei reactions. These reactions can also provide a test validity for new theoretical models.

The ^{10}Be nucleus is a beta decay nucleus with a long half-life of $1.5 \cdot 10^{6}$ years. It has a first excited state 2^{+} at 3.368 MeV and a neutron binding energy is 6.812 MeV [26]. Moreover, a cluster structure ^{6}He+^{4}He has been observed in [27, 28]. Several studies with ^{10}Be at energies around the Coulomb Barrier have been performed [29, 30] allowing to achieve agreement on the inelastic reaction channels. However, the structure of ^{10}Be and its interactions is not yet fully understood and to improve the existing models more experimental data must be obtained [31].

This experiment aimed for the study of the nuclear reaction ^{10}Be+^{120}Sn at energies around the Coulomb Barrier. This reaction allows to investigate the inclusive breakup of ^{10}Be into ^{6}He+^{4}He (Q_{α}=-7.409 MeV) measuring the angular and energy distributions of the ^{6}He and ^{4}He. In addition to this breakup channel, it allowed to measure for the first time the angular and energy distributions of ^{9}Be coming from the ^{10}Be breakup into ^{9}Be+n. Moreover the ^{10}Be+^{120}Sn total reaction cross section extracted from the elastic scattering angular distributions will be

compared with that extracted from the ^{9}Be+120Sn system [32].

The newly developed intense ^{10}Be beam at LNS-INFN [33] presented an opportunity to perform this study where the effects of coupling the inelastic and breakup reaction channels on the elastic scattering. This will lead to useful understanding of reactions induced by the halo nucleus ^{11}Be where the inelastic excitation of the ^{10}Be core has been found to be important to describe collisions involving ^{11}Be [34].

4.2   Experimental Components

The LNS-INFN facility is equipped with a Tandem Accelerator that has a maximum terminal voltage of 14 MV. In this accelerator different ion beams are produced and accelerated. Along the years, from protons to gold, different ions were accelerated where the heaviest could reach kinetic energies up to 200 MeV. The beams provided are used for research in the fields of Nuclear Astrophysics, Nuclear Physics and also for the study of radiation damage in electronics and characterisation of archaeological findings. The Tandem might also be used for the acceleration of Radioactive Ion Beams [35] where isotopes can be extracted either from Sputtering Source or from the Superconducting Cyclotron. In Figure 4.1 it is possible to see a map of the facility with the different elements.
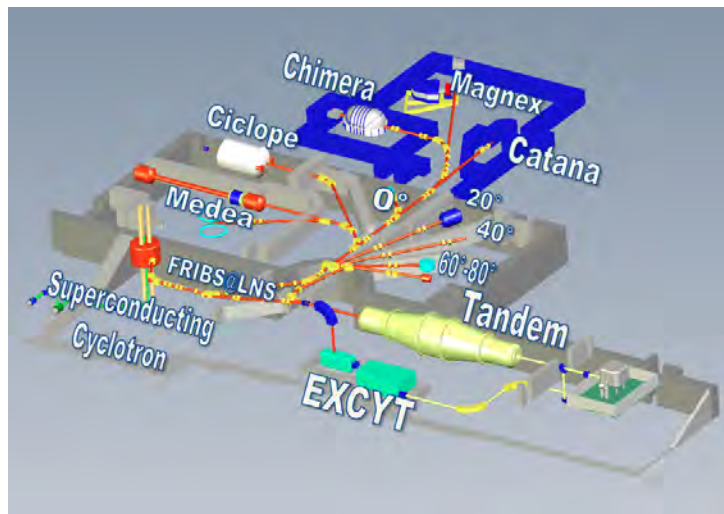
Figure 4.1: Map of the LNS-INFN facility. The different accelerators and elements are presented. The CT2000 scattering Chamber is on the 60° element [36].

Beryllium Beam

During the experiment, both ^{9}Be and ^{10}Be beams were used. These beams are produced by using a similar procedure. The LNS-INFN team developed an intense ^{10}Be beam for injection and post-acceleration in the Tandem [33]. The description on the production methodology provided by P. Figuera et al. [33] is the basis for the description that follows.

The ^{10}Be that are injected in the Tandem accelerator are extracted from graphite targets that have been irradiated with High Energy (HE) Protons at the Paul Scherrer Institute (in

Switzerland) in order to produce muons. The HE protons collide with the target and different isotopes are produced by spallation, including Be isotopes. The mentioned graphite targets have to be replaced every three to four years. Beryllium nuclei can be extracted from these irradiated targets [37, 38] obtaining a solution of $Be(NO_3)_2$ with a ratio ^9Be to ^{10}Be of 2.1.

The chemical process, described in detail in [33], will lead to a solution of BeO to which Ag was added in order to achieve better thermal and electrical conductivity, obtaining BeO:Ag with a ratio of 1:10. This mixture is added to a Cu cathode to be used in the Tandem Ion Source. The cathode is coated with an Au layer to prevent diffusion of Be into the Cu.

The Tandem in the LNS-INFN facility is equipped with a Cs sputter source (Model 860 C, from High Voltage Engineering) where positive ions of Cs are produced. The cathode containing the Be is kept at a potential of -20 kV with respect to the source platform. An electric field between the cathode and the Cs ionizer will puch the Cs ions towards the cathode, extracting the negatively charged BeO that will be injected into the Tandem after a 90° magnet used to select the desired charge-to-mass ratio. The source platform including the 90° magnet is kept at -190 V so that the BeO are injected into the tandem with an energy of (190+20)e = 210 keV. At this stage, the procedure of obtaining a cathode to extract BeO was optimised varying the cone geometry, the ratio of Ag:BeO, annealing procedure of BeO:Ag and the source setting parameters.

When BeO^{-1} is injected into the Tandem it is accelerated in a first phase after which the ionised molecule passes through a carbon stripper foil where the molecule breaks up and the atoms are stripped of some (or all) of their electrons. The positively charged ions are then be accelerated in the second phase of the Tandem. The reported results in the referenced paper measured a charge state distribution of ^{10}Be at the 90° magnet after the Tandem where 13% had charge state +2, 27 % with charge state +4 and the remaining 60% with charge state +3.

These charge states allow ^{10}Be ions to be accelerated at up to 56 MeV in the present Tandem. A $^{10}Be^{+4}$ beam accelerated at 54.4 MeV towards the CT2000 chamber, maximum currents of 9 enA were measured at the entrance of the chamber. The purity of the beam was also analysed with a Telescope Silicon Detector. The beam had a small ^{10}B contamination (which is the product of ^{10}Be decay by β^-) of about 0.15%. The reported ^{10}Be beam intensity is a factor 100 or more larger than what is achieved in other labs (see Table 1 in [33]), making this the most intense ^{10}Be beam known worldwide.

During the experiment were used beams of ^9B, with charge state +2, accelerated at energies of 7, 9 and 27 MeV with intensities of 400 pA. The ^{10}Be beams used had charge state +3 and were accelerated at energies of 7, 9, 27 and 31 MeV with intensities of 200 pA for the two lower energies and ranging from 400 to 1000 pA for the higher energies.

CT-2000 Scattering Chamber

After the Tandem, the beam is taken through a series of magnets towards the 60° beam line that ends in the CT-2000 Scattering Chamber (Figure 4.2). The chamber has a diameter of 2

m and is equipped with two turbo pumps and a cryopump that can bring the pressure of the chamber down to 10^{-6} mbar. There are 16 connection flanges with vacuum feedthroughs with different connectors. Inside the chamber there are two rotating arms that move independently and have a calibrated plate to support detectors, allowing to rotate them during the experiment using step motors. It is also equipped with different collimation systems allowing to measure precise angular distributions [39].

Figure 4.2: Inside view of CT-2000 Chamber. It is possible to see the two rotating arms, some of the flanges with cables and the beam line. On the platform on top of the rotating plate there are two detectors' holding frames.

Targets

During the calibration phase of the experiment, a ^{197}Au target with thickness of 94 μg/cm^2 was used to induce scattering reactions with both ^{9}Be and ^{10}Be beams, at three different energies (7, 9 and 27 MeV) under these conditions, the reaction is dominated by Rutherford Scattering process (both angularly and energetically). The runs at low energies provided the data for the angular calibration of the detector's system and some of the points used for the energy calibration of the SSSDs. The products from runs at higher energy were used for the thickness determination of the thin detectors used in the experiment.

The ^{120}Sn targets with a thickness of 211 μg/cm^2 were used for the main purpose of the BESN experiment. The ^{120}Sn nucleus has fifty protons and seventy neutrons. This nuclear composition reflects a "magic number" of protons (meaning that the proton nuclear shells are completely filled) and an amount of neutrons such that the nuclear levels for neutrons are also completely filled (up to level 1g 9/2) [9]. These characteristics make ^{120}Sn a very stable nucleus and hence with a higher binding energy per nucleon than the one calculated with the semi-empirical mass formula [9]. The chose of such nucleus provides good assurance that target excitations will not contribute to the reaction process, allowing for a cleaner interpretation of te measured angular distributions.

Monitor	Distance (cm)	Angle (°)	Collimator (mm)
M2	91.02 ± 0.1	24.8 ± 0.1	6
M1	91.92 ± 0.1	25.1 ± 0.1	3

Table 4.1: Characteristics of the monitor detectors present in the scattering chamber and used during the experiment. The angle is given with respect to the beam direction, and the distance is provided with respect to the target.

4.2.1 Detection System

The BESN experiment made use of two different types of detectors: monitor detectors and telescope detectors. Monitors were Single Channel Detectors where particles were detected in a single stage. Telescopes instead consistedon a two-staged detector where the particles pass through the first thin layer and stop on the second stage. Below follows a description of these two systems and the electronics that was associated with them.

Monitors: Single Channel Detectors

The detectors used for monitoring the beam position and target composition consisted of two Surface Barrier Detectors with a thickness of 495 μm of Si.

The counts used detectors were placed at such an angle that pure Rutherford Scattering would be measured, allowing for monitoring the beam position, target thickness and number of incident particles. Their main characteristics can be seen in Table 4.1.

Telescopes: DSSSDs and SSSSDs

As mentioned in 4.1, BESN aimed for measuring the contribution and cross-section of different reaction channels. In order to identify the different particles emerging from the reaction it is relevant to distinguish the contribution from different particle's characteristics.

Concerning the dependencies of Stopping Power, expressed in equation (2.4), a possibility for PID arises for Low Energy Heavy Charged Particles, the $\Delta E/E$ Telescope. This detector consists of two stages. The first stage is a thin layer (ΔE) through which the particle will pass through. The thickness of this layer will be chosen depending on the type of particle that will be detected and its energy, in order to assure that the fragments do not stop in this detector stage. Having a look at equation (2.4), where $\Delta E \propto \frac{A \cdot Z^2}{E_{incident}}$, we have that two different particles with the same energy will deposit a different amount of energy in the first stage. Measuring the remaining particle's energy after the thin detector can be done with a thicker detector where the particle will stop. It is then possible to distinguish particles by plotting the energy deposition on the thin layer (ΔE) as function of the total energy deposited in the detector ($E_T = \Delta E + E$). In Figure 4.3 is seen one of these representations with measured fragments at $25°$ from ^{8}He+^{208}Pb reaction at 22 MeV where it is possible to distinguish different particles with the same total energy (events on the same vertical line) due to the measured energy deposited on the first stage of the telescope [24]. The grey dots correspond to simulation data obtained with NPTools package. The circled region corresponds to incomplete charge collection on the inter-strip region of the telescope's first stage.

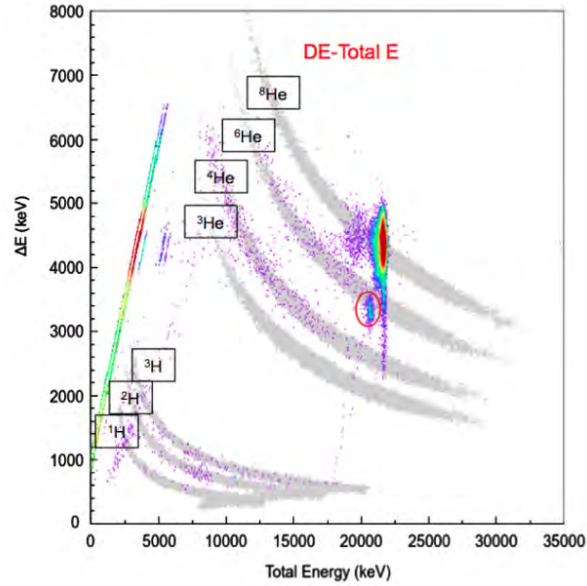In the experimental setup described in this work, the telescopes had a 20 μm SSSSD as the

Figure 4.3: Comparison between simulated (grey dots) and experimental (colored dots) data. The fragments measured come from ^{8}He+^{208}Pb reaction at 22 MeV measured at 25° (laboratory reference frame). [24]

ΔE stage and a 495 μm DSSSD as the E stage (for specifications see Table 4.2). The detectors were mounted in a holding frame that was then fixed to a platform on top of one of the two rotating arms of the CT-2000 chamber. Telescopes were named Telescope A, B C and D. All telescopes had a nominal distance of 88 mm to the target. Telescopes A and B were in the same rotating arm (Arm 1) and placed in the arm at 7.35° and 311° respectively, being measured with reference to the radius that crosses the center of the arm. Telescopes C and D were placed in the second rotating arm (Arm 2) and placed at 356.64 ° and 51.78° respectively, being measured with reference to the radius that crosses the center of the arm. The fully mounted setup can be seen in Figure 4.4.

Architecture	SSSSD	DSSSD
Thickness (μm)	20	500
No. Strips	16	32
Junction Pitch	3.1 mm	3.1 mm
Element Pitch	300.0 μm	300.0 μm
Active Area (mm^2)	50 x 50	50 x 50
Entrance Al DL	0.3 μm	0.3 μm
Entrance Si DL	0.5 μm	0.5 μm

Table 4.2: Specifications of the Silicon Stripped Detectors used in the BESN experiment. Data obtained from [7].

The pixelization of the DSSSDs allows for a fine spatial resolution, each pixel covering a solid angle on the order of 1 msr. For the case of the present work, this pixelization was of great importance for the determination of the thickness of small areas of the SSSSD detectors.

31
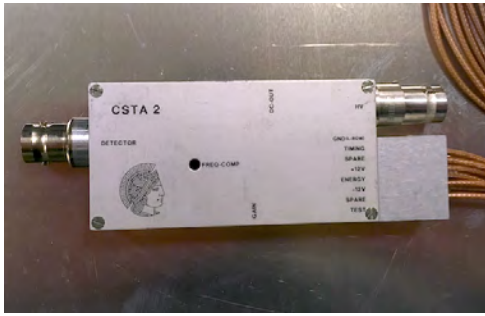
(a)   (b)

Figure 4.5: On the left, a photography of the CSP used for the monitor detectors. On the right a picture of the CSP used for signal coming from the telescopes [40].
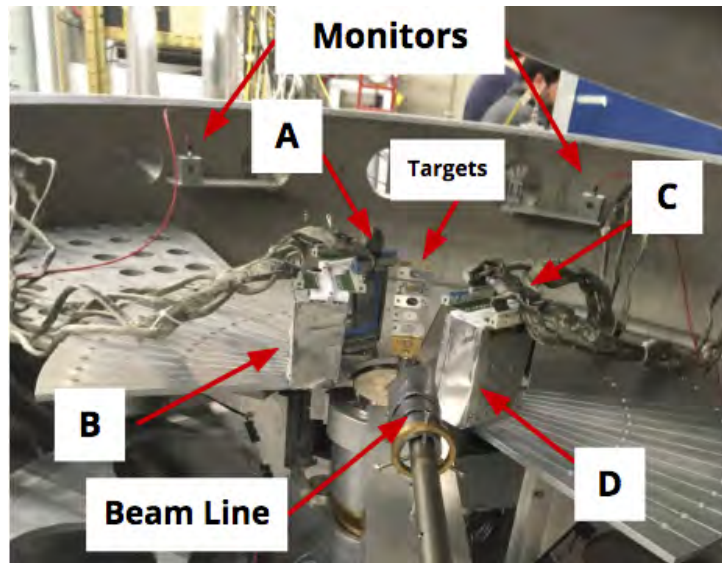

Figure 4.4: Photography with labels of the full setup installed in the CT-2000 Scattering Chamber for the BESN Experiment. The letters on the photography correspond to the telescope identifier letter.

Electronics for Data Acquisition

As discussed previously on 3.2 a particle depositing energy in the depletion region creates e^-/h^+ pairs that when accelerated produce a signal in the electrodes. This signal induces a small current that is firstly sent to *Charge Sensitive Preamplifier* (CSP). In this module the the transient current is integrated in order to produce a voltage step proportional to the measured signal. The CSP used for each monitor was developed by Darmstrad University. For the Telescopes were used MPR-16 CSP's, from Mesytec [40] where each detection unit (SSSSD, Front of DSSSD and Back of DSSSD) was connected to an individual preamplifier. Both models can be seen in Figure 4.5.

The analogue signal outputted by the CSP is sent to the *Spectroscopy Amplifiers*. In this module the voltage step sent from the CSP is converted into a pulse with height proportional to the measured signal while filtering low and high frequency noise. The generation of this pulse is not instant but in order to avoid overlapped signals the rise time and the time it takes to go back to the base line must be low. However, if this time is shortened too much it will
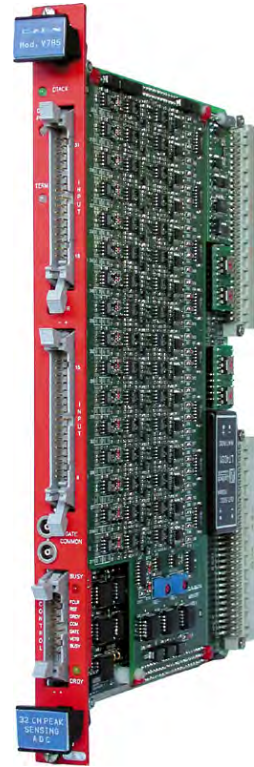
(a)   (b)

Figure 4.6: On the left, MSCF-16 Amplifier used for processing the signal from monitor detectors [41]. On the right, V785 ADC module used for converting the analogue signals from amplifiers into digital signal [42]

allow more high frequency noise to to influence the processing of the signal. As the measured signal is proportional the energy deposited in the active material of the detector, the generated peak will have an height proportional to the energy deposited. These modules, which have 16 independent amplification channels, also make signal discrimination emitting a logic signal if one of the 16 strips in input generates a signal above the programmed threshold. For the setup used, the Amplifiers for processing of the signal from the telescope systems were Megamp modules developed by INFN-Milano, while the one used for the monitors was a MSCF-16 F module from Mesytec [41] (See Figure 4.6(a)).

After the Amplifier, the signal is ready to be digitalized by an *Analogue Digital Converter* (ADC) module. This module converts the signal form the Amplifier into a digital signal with the same information but now readable by a central process unit (CPU). The ADC converts the analogue signal from the amplifier once it receives a logic signal from the Gate Generator, which is a module in the logic circuit that makes the ADC process information during a certain time interval. In this experiments, the ADCs used were V785 modules (see Figure 4.6(b)) from CAEN [42].

The total schematic diagram for the electronics associated with the analogue signal measured in each detector is seen in Figure 4.7

The selection of events to be recorded in the CPU is done by a logic circuit. The amplifiers emit a logic signal when any of the channels being read in that unit measures a valid event
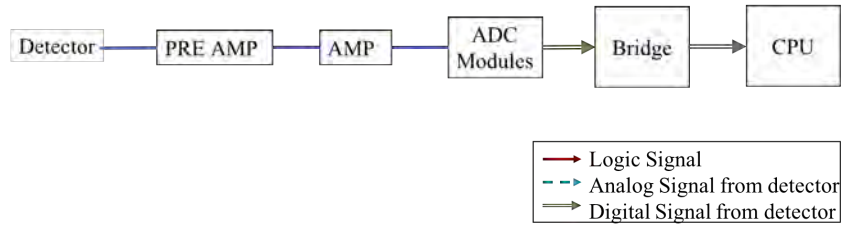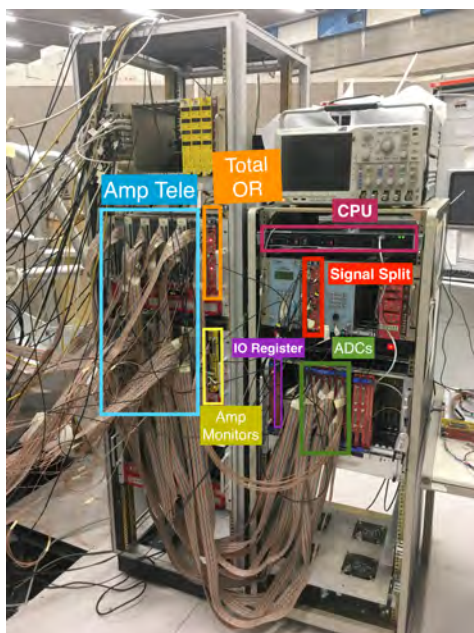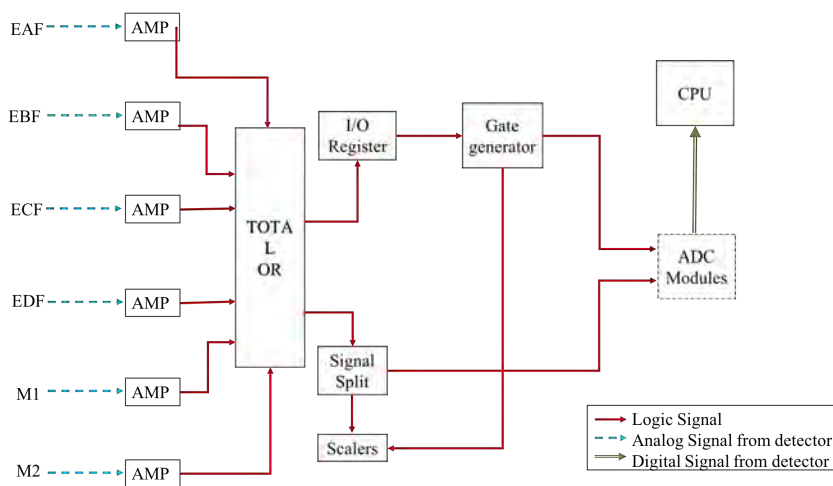
Figure 4.7: Schematic Diagram of the electronics for processing the measured analogue signals, from detection to delivery in the CPU. PRE AMP is a CST and AMP for the spectroscopy amplifiers.

(according to the thresholds set in the amplifier). In this work, the logic signal from amplifiers of all DSSSD front detectors and monitors was sent to a *Fan in/Fan Out* module (FIFO), a N454 logic module from CAEN [43] that outputs the Total OR of up to two sets of eight inputs and splits it up to eight equal outputs.

From the Total OR, the signal is split in two. One of these signals is sent to an *Input/ Output Register* (I/O Register), in this work was used a V977 from CAEN [44]. When this happens and the systems generates at the output of the I/O Register a signal that is sent to the Gate Generator (GG), which was a GG8000. The signal generated by the GG is then sent to the Gate input of the ADC's, opening a time window the signals received from the amplifier to be converted and sent to the CPU. The second signal coming from the Total OR is sent to a scaler to count the total number of valid events. In Figure 4.8(a) is seen the rack of the experimental room set for the BESN experiment. The sketch of the logic signal diagram is presented in Figure 4.8(b).

(a)

(b)

Figure 4.8: On the left, a photography of the rack with the electronic modules set for the BESN experiment. On the right, a schematic diagram of the electronics for processing the logic signals.

Chapter 5

Characterization of SSSSDs thicknesses and its impact on experimental analysis

The main goal of this work is to determine the effective thickness of the SSSSDs used in the BESN experiment in order improve the resolving power of the detectors and thus reduce the uncertainty in the results from the data collected during its execution. Several tasks had to be performed and are described in this chapter. Some experimental details influence this analysis, therefore a detailed approach to each task was taken in order to reach a precise characterization and improve the detectors' energy resolution.

5.1   Configurations of detectors and coincidences

The analysis of the geometry defined for the BESN experiment is of most importance in order to characterize the thickness of the thin Si detectors as the measurements performed for the thickness calculation depend on aspects such as coincidences between the detectors and positioning of the detectors. The experimental setup (described in Section 4.2) had the four telescopes disposed in two rotating arms that were used to arrange the setup in three different configurations (Table 5.1)

Telescope	Standard Configuration	Configuration 2	Configuration 3	Full Coverage
Telescope A	60.00°	50.00°	60.00°	34° - 76°
Telescope B	115.35°	106.35°	116.35°	90° - 133°
Telescope C	85.00°	85.00°	75.00°	59° - 101°
Telescope D	140.14°	140.14°	130.14°	114° - 157°

Table 5.1: Angular position of the center of each telescope with reference to the beam direction, for the three different configurations considered in the experiment. The angular uncertainty for the position of each telescope is 0.01° due to precise measurements on the position of the arms.

These three configurations were used to cover a wider angular range and simultaneously to prevent Detector B from being in the shadow of the target frame, as seen Figure 5.1. In this Figure the detectors are displaced as in Standard Configuration and the target is tilted 45°. When Configuration 2 is used, this detector comes out of the shadow of the target's frame.
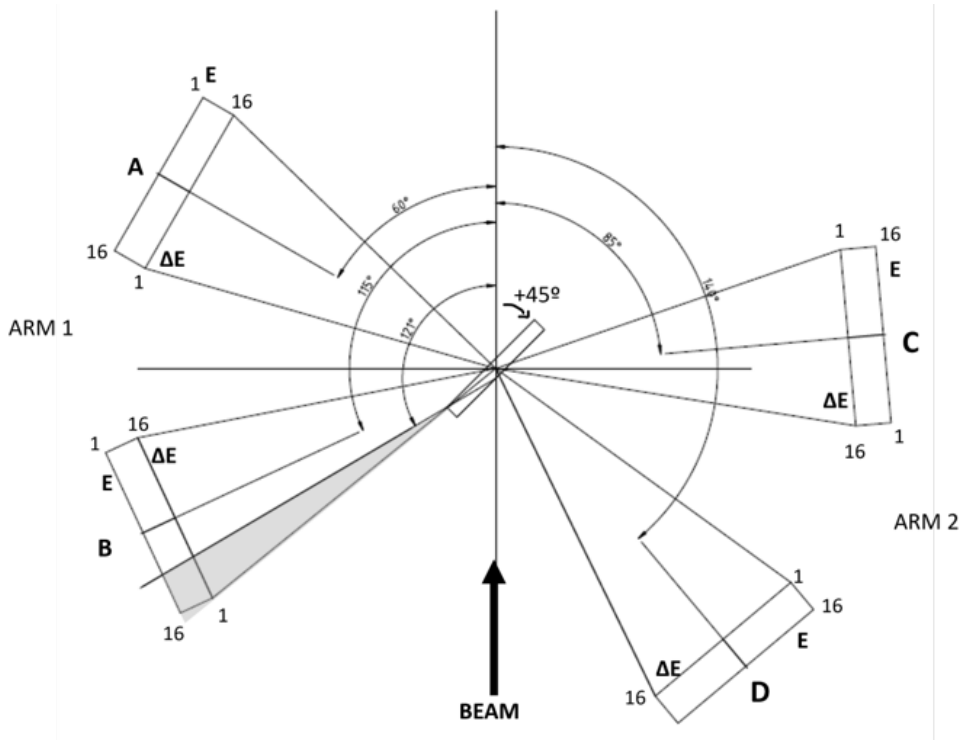
Figure 5.1: Sketch of Standard Configuration for the BESN Experiment. The numbers show the orientation of the vertical strips of each detector and the shadowed region on Telescope B enhances that in Standard Configuration this region of the detector is in the shadow of the target and target frame. The target tilt is also dispalyed as well as the detectors' angles. Adapted from the experimental log book.

Several details on this sketch are important for the analysis. The orientation of the strips of the two stages of each telescope, the orientation of the 45° tilt of the target and the limit angle after which detector B is in the shadow of the target frame.

The two stripped detectors of each Telescope were mounted in a way that the distance between frontal plane of each detector is of 20 mm, as seen in Figure 5.2. This distance is crucial to understand the coincidences in the Telescopes.

Concerning the coincidences between the two stages of the telescopes and the orientation of the strips, it would be possible to admit in a first approach that a particle passing through strip i of the thin detector would cross the vertical would as well hit the strip vertically aligned in the thick one. This would be the case if the particles hit the detector perpendicularly to its surface. However, the particles detected in this experience were coming radially from the beam spot on the target which results in particles not hitting the detectors perpendicularly to their surface. As seen in Figure 5.3, with the target at a distance of 80 mm, particle trajectories can describe an angular opening of 17° with respect to the central normal incidence. Projecting this angle along the 20 mm distance between thw two detectors, results a lateral deviation of 6.1 mm. This is of great relevance, as the pixels in the E detector do not correspond directly to a perpendicularly projected pixel on the ΔE detector. Another consequence is that none of the particles crossing the first stage of the Telescope close to its boarders will not be detected on the second stage, limiting the detectors area that can be characterized in thickness.
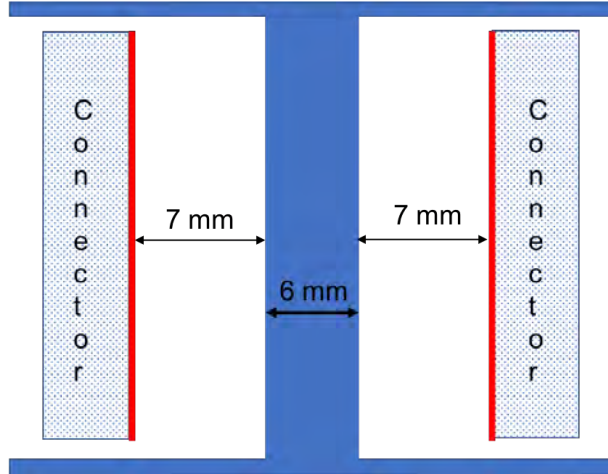
Figure 5.2: Top view of the Telescope connectors scheme. The Detectors plane is in red and the holding frame in blue. Adapted from the experimental log book.
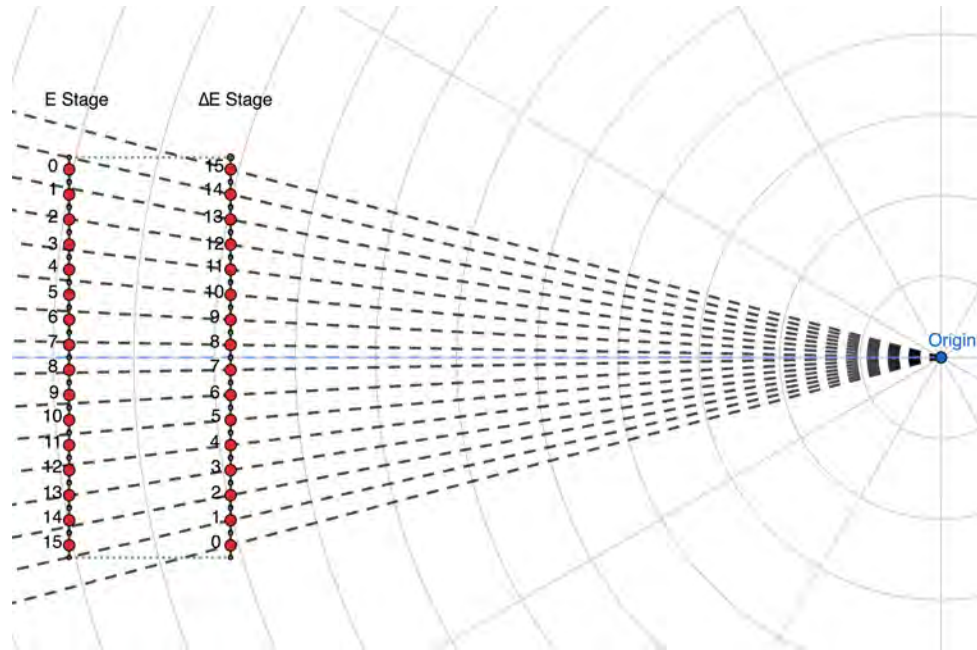
Figure 5.3: Trajectories (dashed lines) of particles detected with a telescope detector at the BESN experiment. The red dots correspond to the center of each vertical strip, the blue dashed line is the trajectory of particles coming perpendicularly to the detector's plane. The indexes correspond to the vertical strip indexes.

5.2   Angular Calibration

The first step done in the analysis was the verification of the angular position and orientation of the detectors. Further steps on the analysis heavily on the angular adjustments performed due to changes in the effective thickness of the active and dead layers of the detectors.

The angular calibration relies on analysing the angular distribution of a Rutherford Scattering reaction, with ^{10}Be at 27 MeV being scattered in ^{197}Au. The distribution follows (2.21) and it is possible to reach a precise configuration of the setup by adjusting the position and orientation of the detectors. Experimental runs of this reaction with setup in configuration 2 were used in

38

order to remove telescope B form the targets shadow. For the other telescopes was used runs in standard configuration.

The adjustments on the detectors positioning and orientation made use of two reference frames. The chamber's reference frame has its origin on the point were the beam hits the target. The z-axis has the direction of the beam, the y-axis is on the vertical direction of the target holder and the x-axis on the horizontal with respect to the target holder. The second detector's reference frame has its origin in the middle of each detector where the z-axis is in the direction of the normal to the detectors plane (from target to detectors plane), the y and x-axis are along the vertical and horizontal axis of each detector. The position and orientation adjustments were done by varying geometrical parameters:

- **d:** distance of the detector to the target

- **θ:** angle at where the center of the detector sits in the chamber with reference to the beam line

- **θ_y:** tilting angle on the vertical axis of the detector

The adjustments were achieved by firstly transforming the coordinates of each pixel of the DSSSD into the reference frame of the detector by applying:

$$
\begin{cases} x_1 = x - x_0 \\ z_1 = z - z_0 \end{cases} .
\tag{5.1}
$$

where x_1 is the position (in the $0x$ axis of the detector) of the center of the pixel with reference to the center of the detector, x is the position along the x-axis in the reference frame of the chamber and x_0 being the position of the center of detectors reference frame in the x-axis of the chamber's reference frame. Same definition applies for the z_i variables. To these new coordinates, in the reference frame of the detector, Euler Transformations along the y-axis of the detector's reference frame were applied to all the pixels' new coordinates (x_1 and z_1) by using

$$
\begin{cases} x_{new} = x_1 cos\theta_y + z_1 sin\theta_y + x_0 \\ z_{new} = -x_1 sin\theta_y + z_1 cos\theta_y + z_0 \end{cases} .
\tag{5.2}
$$

where x_{new} and z_{new} are the new positions along each respective axis in the detectors reference frame and θ_y is the tilting angle to be applied. Going back to the chamber reference system can be achieved by applying (5.1) to the new coordinates.

For the adjustments of the positioning and orientation of the detectors, the elastic scattering peak measured in each pixel of the DSSSD was integrated from peak centroid $\pm$ 3 standard deviations of a gaussian function fitted into that area of the spectrum. The Rutherford differential cross section (2.24) depends on some characteristics experimental run (such as the charge and the energy of the beam particles) and on the $cosec^4 \left(\frac{\theta'}{2} \right)$. Comparing it with equation (2.20) it results that:

$$
\frac{dR_b}{4\pi I_a N_t} = K(Zze^2)^2 \left(\frac{1}{4T_a} \right)^2 cosec^4 \left(\frac{\theta'}{2} \right)
\tag{5.3}
$$

39

where dR_b is given by the detected particles at a given θ over a solid angle $d\Omega$, N_{count}. This brings that:

$$r(\theta, d\Omega) = \frac{N_a}{A} 4\pi N_t K (Zze^2)^2 \left(\frac{1}{4T_a}\right)^2 \tag{5.4}$$

where r is given by:

$$r(\theta, d\Omega) = \frac{N_{count}}{cosec^4\left(\frac{\theta'}{2}\right) d\Omega} \tag{5.5}$$

all the dependencies of r are measurable experimental parameters, where θ' is obtained by the conversion of θ through equation (2.18). On the other hand, the right side of equation (5.3) is dependent only of characteristics of the reaction, meaning that this value r should be the same for all pixels in a detector, since the data used was from an elastic scattering reaction. With the elastic peak integrals from each pixel, a Python program was developed in order to adjust the mentioned parameters for the whole detector and calculate both the central angle and solid angle of each pixel after the changes are applied. By varying the geometric parameters the mentioned the ratio in each pixel is changed and a minimization over the relative squared error of the distribution of $r(\theta, d\Omega)$ with reference to the expected estimated with 2.21 one should be able to achieve a better estimation of the position and orientation of the detector.

This minimization was done by varying the geometric parameters in an isolated way within a certain range. For each of step the relative squared error to the average of the distribution, β, was calculated using:

$$\beta = \sum_{i=0}^{p} \frac{(\bar{r} - r_i)^2}{\bar{r}^2} \tag{5.6}$$

where $_i$ is the index of the pixel, p the total amount of pixels and $\bar{r}$ is the average value of r for the distribution.

Having varied all the parameters over their range, the one that lowered β the most is set to that value. This process was iterated, reducing the range of values over which the last changed variable runs through in order to make finer adjustments in each iteration. The process would conclude when the best parameter change induces a meaningless reduction of β (less than 1% of the previous value of β). In Figure 5.4 is seen β as a function of the different adjusted parameters in the last step of optimization. It is also represented the distribution of r before and after the adjustments.

The final position and orientation of the detectors is presented in Table 5.2. From this table is relevant to mention that the change in d for DSSSD B was significant. It represents an unexpected correction of the setup. All DSSSDs were characterized following the same procedure, however, due to the shadow covering DSSSD B standard configuration, this was the only detector making use of data from a different run, where the configuration brought the whole detector out of the shadow. Further discussion over this value of d and its causes must be assessed by the collaboration.

Detector	d_i (m)	d_f (m)	$\theta_i(°)$	$\theta_f(°)$	$\theta_y, i(°)$	$\theta_y, f(°)$
A	0.108	0.107	60.00	60.00	0.00	2.38
B	0.108	0.093	106.35	106.35	0.00	-1.50
C	0.108	0.108	-85.00	-82.25	0.00	0.15
D	0.108	0.108	-140.00	-140.00	0.00	4.25

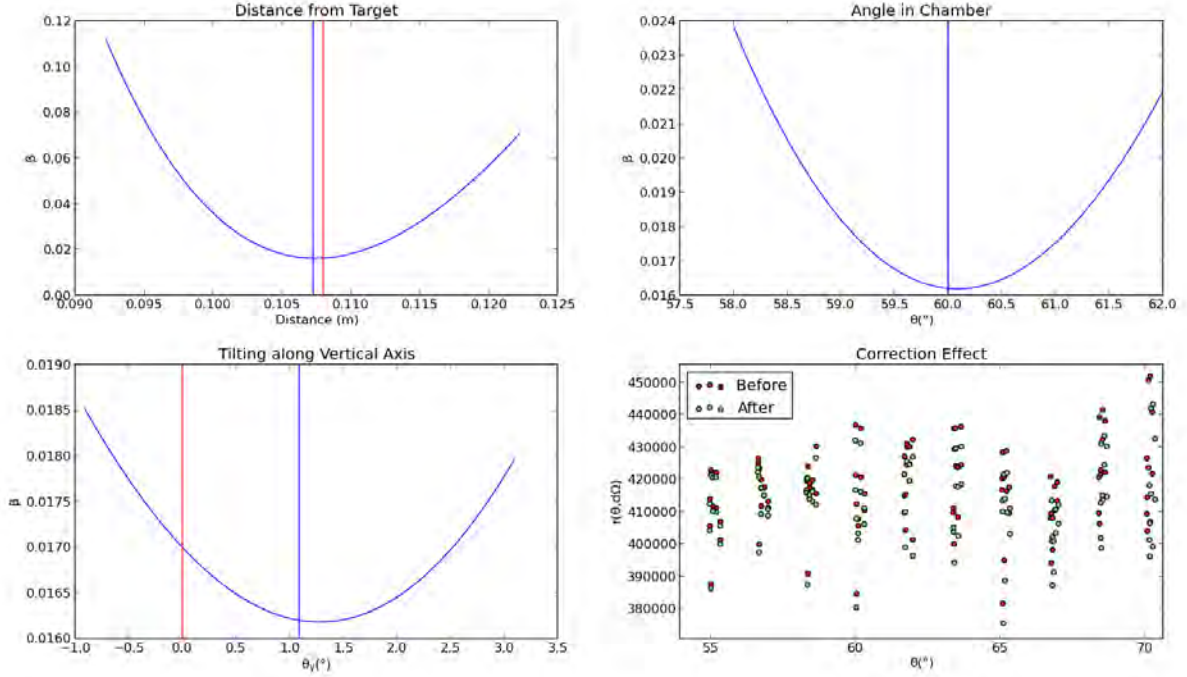Table 5.2: Change in distance, θ and θ_i due to Angular Calibration

Figure 5.4: Last step of minimizing β by adjusting the positioning of DSSSD A. In each graphic, the red vertical line corresponds to the initial value of the parameter and the blue vertical line corresponds to the final value of the parameter. The graphic on the bottom right shows the $r(\theta, d\Omega)$ distribution before and after the corrections.

5.3 Energy Callibration DSSSD

The energy calibration of the DSSSDs was performed with the use of a standard triple-α source with ^{239}Pu, ^{241}Am and ^{244}Cm isotopes. The most intense α-particles emitted by these isotopes are described in Table 5.3

Isotope	Half-life (y)	Energy (keV)	Emission Probability
^{239}Pu	24110	5156.59	73 %
		5144.3	15 %
^{241}Am	432.2	5485.56	84.5 %
		5442.8	13.6 %
^{244}Cm	18.1	5804.82	76.4 %
		5762.70	23.6 %

Table 5.3: Most intense alphas emitted from triple-α source [45] used for energy calibration of the DSSSDs.

The spectra obtained by each strip of the DSSSDs when directly exposed to the triple-α

source (Figure 5.5) were used to convert electronic channels from the Data Acquisition System into energy deposited in the active material of the detector. In Figure 5.5 the six peaks of the mentioned most intense α-particles are seen. These spectra include the events that produced signal in only one Front strip and one Back strip, filtering some of the eventual noise in the Front or Back side. A program was developed using *Root* [46] for the energy calibration of all the Front and Back strips of the four DSSSDs. This program allowed the selection of each of the six peaks centroids for each strip's spectrum, proceeding with fitting six gaussian functions initially centered in the selected centroids. A linear regression is done over the points E_α(centroid), taking only into account the three more intense α-particles from this source. The parameters of this regression are then used as calibration parameters to convert channels into energy for events in the DSSSD.
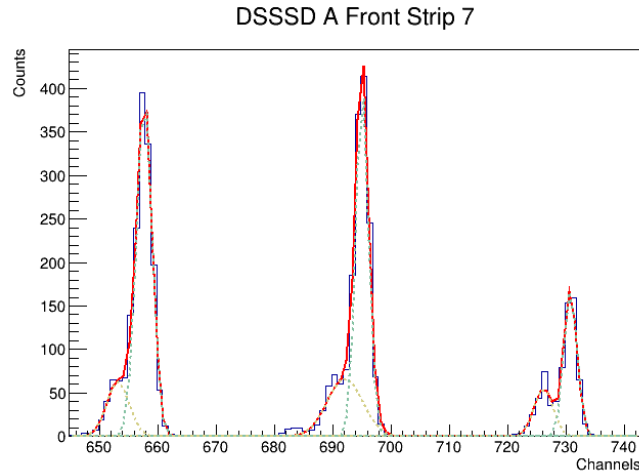

Figure 5.5: Spectrum measured with in the front strip #7 of the DSSSD from Telescope A when exposed directly to the triple-α source. The red line is the sum of the six gaussian fits performed in this region of the spectrum (coloured in yellow and green).

Gain Match

A passing particle in a DSSSD will produce an equal amount of electrons and holes. It is then expected that, selecting the events with the condition previously stated and assuming that all the charge is collected, the spectra comparing the energy measured in the Front with the energy measured in the Back strips would be a straight line where $E_{Back} = E_{Front}$. This was not observed when adding data of the events from a run with the triple-α source with a run from ^{10}Be scattering in ^{197}Au at the energy of 27 MeV. In some spectra, as the measured energy increased, the difference $\|E_{Back} - E_{Front}\|$ also grew, even though the relation between the two measured energies was kept linear (Figure 5.6(a) and Figure 5.6(c)). As the main objective of the DSSSD in this work was to select the relevant events for the thickness determination of the SSSSDs the calibrations were adjusted in order to account for possible gain difference between the Back and Front strips.

The correction was done by analysing each pixel's representation of E_{Back} vs E_{Front} and map the pixels where $E_{Back} = E_{Front} \pm 0.2$ MeV, for example, in Figure 5.6(a) it is seen that the representation does not follow the condition. A reference strip is chosen when it does follow

the condition except in pixels defined by the reference strip and a strip that does not follow the condition in any of its pixels. For simplicity, let us assume that the reference strip is from the Back of the detector. Once a good calibration is achieved it is possible to apply a criteria over the energy difference measured on back and front strips in each event. This allows to get rid of interstrip effects, where the charge is not completely collected.
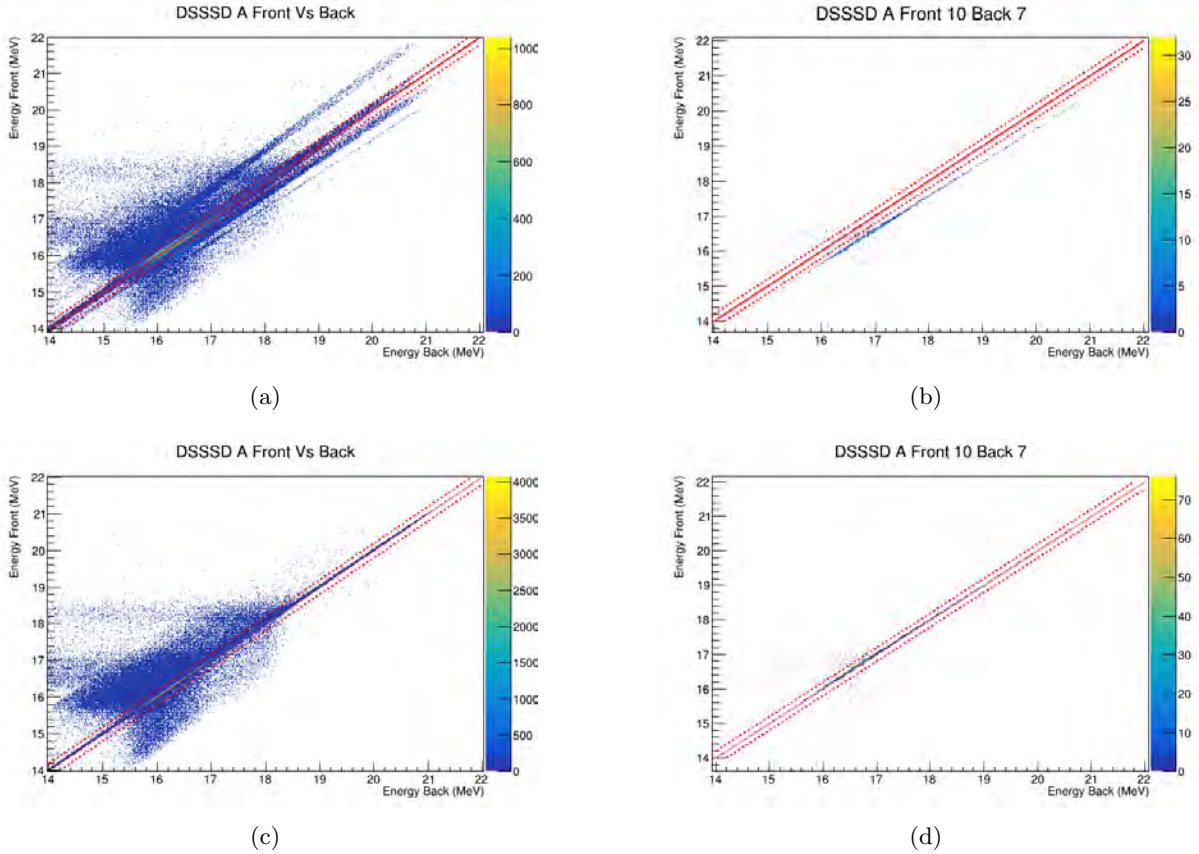

(a)

(b)

(c)

(d)

Figure 5.6: Energy measured in the DSSSD A front strips vs the measured in the back strips of same detector. In (a) and (c) for the whole detector, before and after the gain match correction, respectively. In (b) and (d) for a single pixel defined by the signals obtained simultaneously in Front strip #10 and Back strip #7

For this procedure, each pixel's spectra is analysed with data from the exposure of the detector to triple-α source and particles from the reaction of ^{10}Be with ^{197}Au at the energy of 27 MeV. A mapping describing whether the representation of the energy measured on one strip as a function of the energy measured on the other strip describing the pixel fell within a region of $E_{Back} = E_{Front} \pm 200$ keV. A reference strip was selected based on this map and for simplification of the explanation let us consider that it was a Back strip. The representation of E_{Front} vs E_{Back} is done for each pixel along this reference strip where the measured energy on the reference strip is kept on the Vertical Axis and the Horizontal Axis has the measured energy on the second strip that defines the pixel. The events from the straight line are selected and E_{Front} vs E_{Back} is redrawn with the horizontal axis in channel units. A new calibration of the Back strip is done with reference to the energies measured on the reference strip. Once all the Back strips are re-calibrated, the Front strips follow the same procedure, having that in the Vertical Axis now is the energy measured on all the Back strips and in the Horizontal Axis the spectrum measured in a single Front strip.

By doing it so was possibly to readjust the calibration so that the energy resolution of the whole detector improves (compare graphics from Figure 5.6), allowing to select the valid events with an energy condition where $E_{Back} = E_{Front} \pm 3\sigma_{diff}$, where σ_{diff} represents the standard deviation of $E_{Back} - E_{Front}$. The analysis of the dispersion between the energy measured in the Back and Front strips of the DSSSD was done before and after the gain match process (See Figure 5.7). In Table 5.4 is seen the impact that the gain match had on the coherence between the energy measured in the Back and Front strips of the DSSSDs.

DSSSD	σ_{diff} (keV)		μ_E (keV)	
	Before	After	Before	After
A	590.00	15.83	11.70	-3.26
B	28.29	13.30	-17.71	4.26
C	36.57	15.11	-20.08	5.24
D	25.00	13.14	14.99	2.86

Table 5.4: Comparison between σ_{diff} and mean value (μ_E) of the distribution of the $E_{Back} - E_{Front}$.

It would be expected that the μ_E values after the gain match would be zero, as all the strips were re-calibrated with reference to the same strip. The values presented for μ_E after gain match depend on the chosen reference strip. Even with this re-callibration biased to the strip chosen as reference, the improvement of energy resolution is understandable from the change in σ_{diff}.
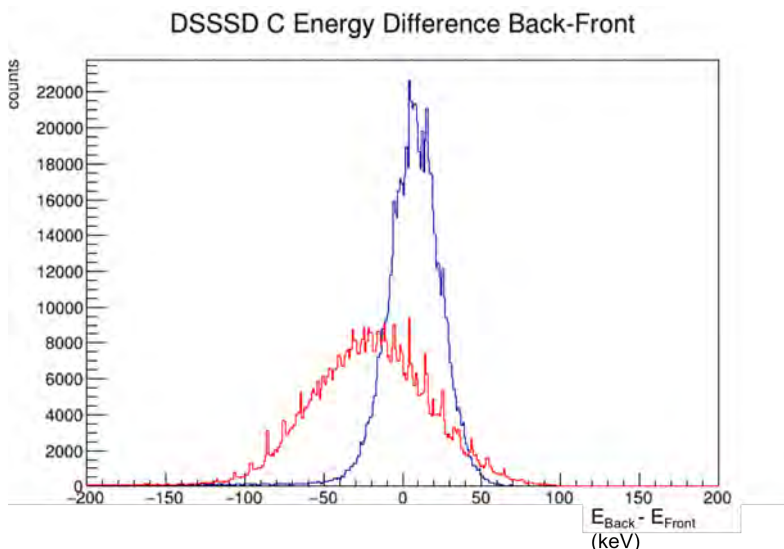
Figure 5.7: The distribution of $E_{Back} - E_{Front}$ in DSSSD C before (in red) and after (in blue) the gain match

It is important to stress that for the purpose of this work, the main function of the thick detectors is to select the relevant events for the thickness determination of segments in the thin detectors rather than accurately measure the energy that particles deposit in the detector. Therefore, the gain matched allowed for a better selection of events by reducing σ_{diff}, the

parameter used for defining the maximum difference between the energy measured in E_{Back} and E_{Front} to consider an event as valid.

5.4   Energy Calibration SSSSD

To measure the thickness, μ of the active layer of the SSSSD it is important to measure the energy deposited by particles in this layer, which makes an accurate calibration of each strip crucial.

To calibrate the thin SSSSSDs a ^{148}Gd source, that emits an α-particle of 3.183 MeV, and the products from two different nuclear reactions were used. These reactions were the scattering of ^{10}Be at the energies of 7 and 9 MeV on a thin foil of ^{197}Au. The spectra measured in each strip when exposed to the different particles was analysed and the mean of the most predominant peak was determined by fitting a Gaussian function. These were the values in channels used to calibrate the detector. The energies corresponding to each peak were estimated using three different approaches.

5.4.1   Nominal energies approach

In this first approach, it was consider that the mean of the peak in the spectrum of each strip corresponds to the nominal energy of the particles. The particles from the scattering follow an energy distribution ruled by equation (2.21). Considering each pixels' central θ it was possible to calculate the energy of the particles emitted with that angle.

5.4.2   Energy loss in material approach

As discussed in 2.1, when passing through material, heavy particles loose energy by different interactions with the material. For the energy estimation of the particles used to characterize the SSSSSDs this loss of energy on the different layers must be calculated, knowing that in dead layers the energy loss is not measurable. The considered non active material was the target itself, the Al layer in the SSSSD and the non active Si. The reaction was consider to happen in the middle of the target, correcting the energy at which the reaction happens.

Even though the Stopping Power follows equation (2.4), its value was assumed to be constant along the path of the particle in each layer, as the energy loss in such small thicknesses (fractions of μm) would not change considerably. Using SRIM [47] it was possible to obtain Stopping Power tables and, with interpolation, the Stopping Power of a given particle at the energy before crossing that layer (E_{before}) of known composition was estimated. With these considerations, the energy of the particle after passing through a layer (E_{after}) is estimated by

$$E_{after} = E_{before} - S(E_{before}) \times \mu_{nominal} \tag{5.7}$$

In this approach the alpha-source was considered a punctual source sitting in the target frame and that the scattering reactions would occur in the middle of the ^{197}Au target. For the case of scattering reactions, these would occur after the beam passed through half the target

thickness and the particles coming out of the reaction would have to cross the remaining gold thickness. Before reaching the active material of the SSSSD, the particles would still have to cross the Al and Si dead layers of the detector.

5.4.3 Energy loss in material with entrance angles approach

The last approach considers the effective thickness that the particles crossed in each layer. Due to the fact that these particles stop in the active material of the SSSSD, the spatial discretization was limited to vertical strips. The entrance angle was calculated as the angle done by the vectors with origin in the center of the target pointing to the center of the considered strip and to the centre of its detector.

The effective thickness (μ) is geometrically given by:

$$\mu = \frac{\mu_{nom}}{|cos(\theta_{det} - \alpha_{target})|} \tag{5.8}$$

where μ_{nom} is nominal thickness of the layer, θ_{det} is the angle at which the strip is and α_{target} is the tilted angle of the target. To obtain the effective thickness that the particle passed through before reacting in the target, θ_{det} is set to $0°$. For the effective thickness of a layer after the target θ_{det} is substituted by the entrance angle while $\alpha_{target} = 0°$. The energy of a particle after passing through a layer is therefore given by equation (5.7) where $\mu_{nominal}$ is substituted by μ.

For the calculations with the α-source it was considered as a point source tilted at $45°$ for the runs used to calibrate detectors A and D and $-45°$ for the runs used to calibrate detectors B and C.

The scattering reactions used for the calibration of the SSSSDs had the target tilted by $45°$. Therefore, a ^{10}Be particle would cross half of the effective thickness before interacting with the 197Au target. The energy of the particle before reacting is therefore corrected by its reduction due to interactions with half the material thickness.

The energies obtained from the three approaches were calculated with a Python program (continued version of the Python code previously mentioned in Section 5.2 that integrates the needed operations mentioned in this Section) and are represented in Figure 5.8. For the scattering runs the second approach shows a relevant change (about 8 %) in the energy of the particles reaching the detector, whereas the third approach shows more relevance for the runs with the α-source correcting energies of emmited α-particles from 3.183 down to 2.928 MeV. The behaviour seen in Figure 5.8(c) is due to the big entrance angle differences when considering a point source.

5.5 Thickness Determination

The same reaction used for the Angular Calibration (^{10}Be at the energy of 27 Mev with a ^{197}Au target) was used for the characterization of the thin detectors' thicknesses . The ^{10}Be
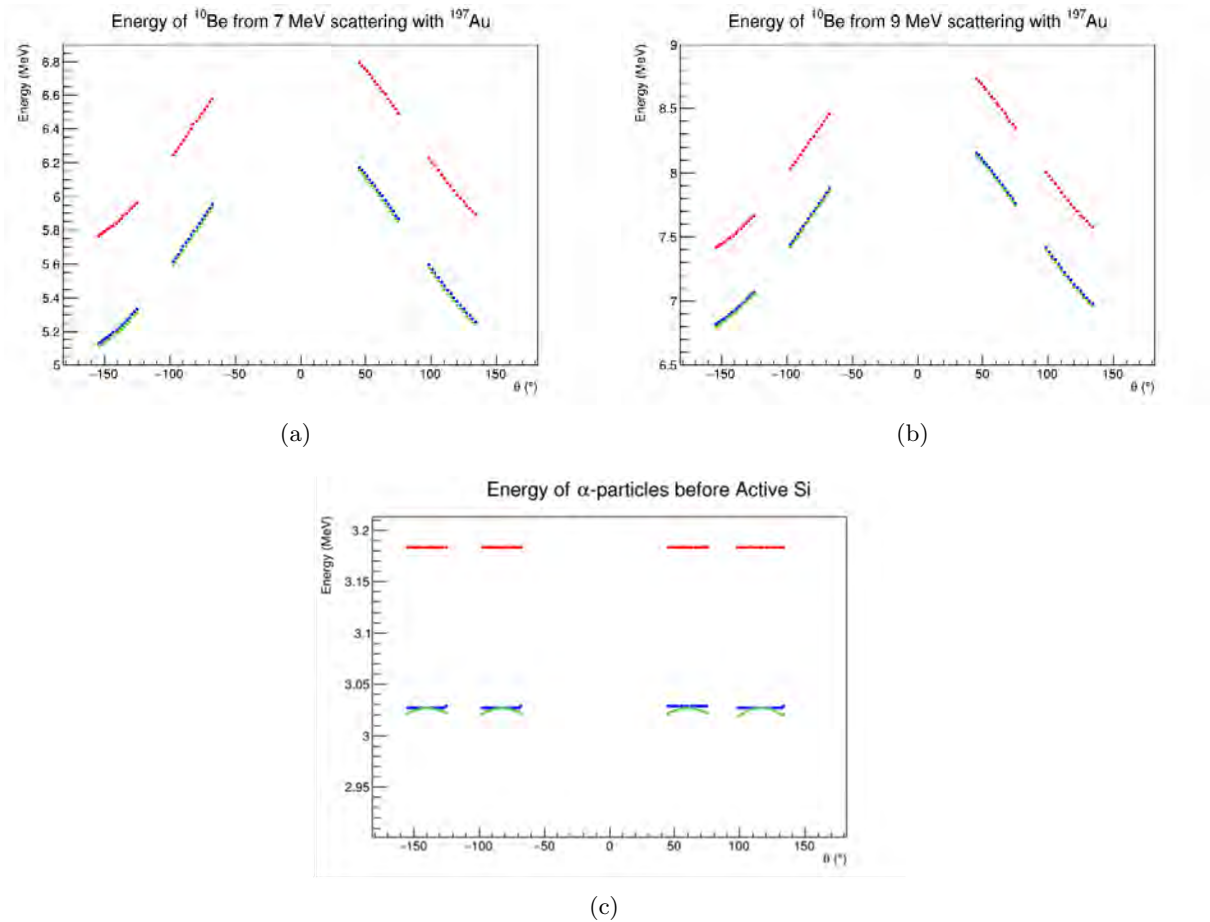
(a)

(b)

(c)

Figure 5.8: Energies of the different particles used for calibration of the SSSSD obtained by the three different approaches considered. In red energies from the nominal energies approach, in blue from the energy loss in material approach and in green from the energy loss in materials with entrance angles approach.

scattered particles reach the active material of the different detectors with energies ranging from 26 MeV to 21.9 MeV, according to calculations performed as described in Section 5.4. At this energy regime, the particles punch through layers of Si with thickness below 40 μm (according to Projected Range tables from SRIM [47]).

The second stage of the telescopes was used to determine the angle at which the particles were emitted, thus allowing for a spatial distribution of the energy deposited by the particles in the SSSSD. The pixelated detectors were also used to select events. These would be considered valid if the difference between the energy measured in front and back strips would not differ more than 3σ, if the energy measured in the thick detector was greater than 200 keV and if the signal in the SSSSD was greater than 200 channels, due to the offset of the calibration. To simplify the analysis, only events with multiplicity 1 were considered. Histograms were filled with this selection of events for each pixel with the energy that was deposited in the SSSSD. Most of these spectra had a single peak which corresponded to events of particles coming from the scattering that deposited an energy in the SSSSD corresponding to the mean of that peak. Along some vertical strips of DSSSD D, two peaks were observed at different energies, for the energy deposited in the corresponding SSSSD. The case was analysed and the sum of the integrals

of both peaks was in the order of magnitude expected for the integral of a single peak, when compared with other pixels where a single pixel was measured. This can be related to some eventual gain shift problem in these strips of SSSSD D. The thickness calculated for double-peak cases took into account the most intense peak, however, it is known that due to this problem it is mostly probable that it will not present a reasonable value.

The estimation of the thickness through which a particle hitting a certain pixel of the DSSSD crossed in active material of the first stage of the Telescopes was done by further development of the previously mentioned Python program. This calculation followed two different approaches. One where the Stopping Power was considered to be constant along the path in the active layer of Si. The other follows the approach adopted by [22] that uses the ranges of ^{10}Be in Si at different energies.

5.5.1   Constant Stopping Power approach

From the tables provided by SRIM it is seen that the Stopping Power for ^{10}Be in Si at 27.5 MeV is of 0.3509 MeV/μm and at 20 MeV is of 0.4209 MeV/μm, representing an increase of 16% for a decrease in 25% of the energy. The energy loss in the SSSSDs ranges from 5.6 MeV to 10.4 MeV, which can lead to a change in the Stopping Power along the path in the active material of up to 20%. Even though the reduction of the Stopping Power is considerable, the energy deposited in the thin layers that the particles punch through will be relatively small compared with their total energy.

This approach looks for an estimation of the thickness based on a constant Stopping Power. Using (5.7) and applying that $E_{loss} = E_{before} - E_{after}$ comes that

$$\mu = \frac{E_{loss}}{S(E_{before})} \tag{5.9}$$

which estimates the effective thickness that the particle passes through in the active material of the thin detector. Correcting with equation (5.8), the nominal thickness of active Si in the SSSSD that the particles reaching a pixel of the DSSSSD crossed is obtained. (see Figure5.9)
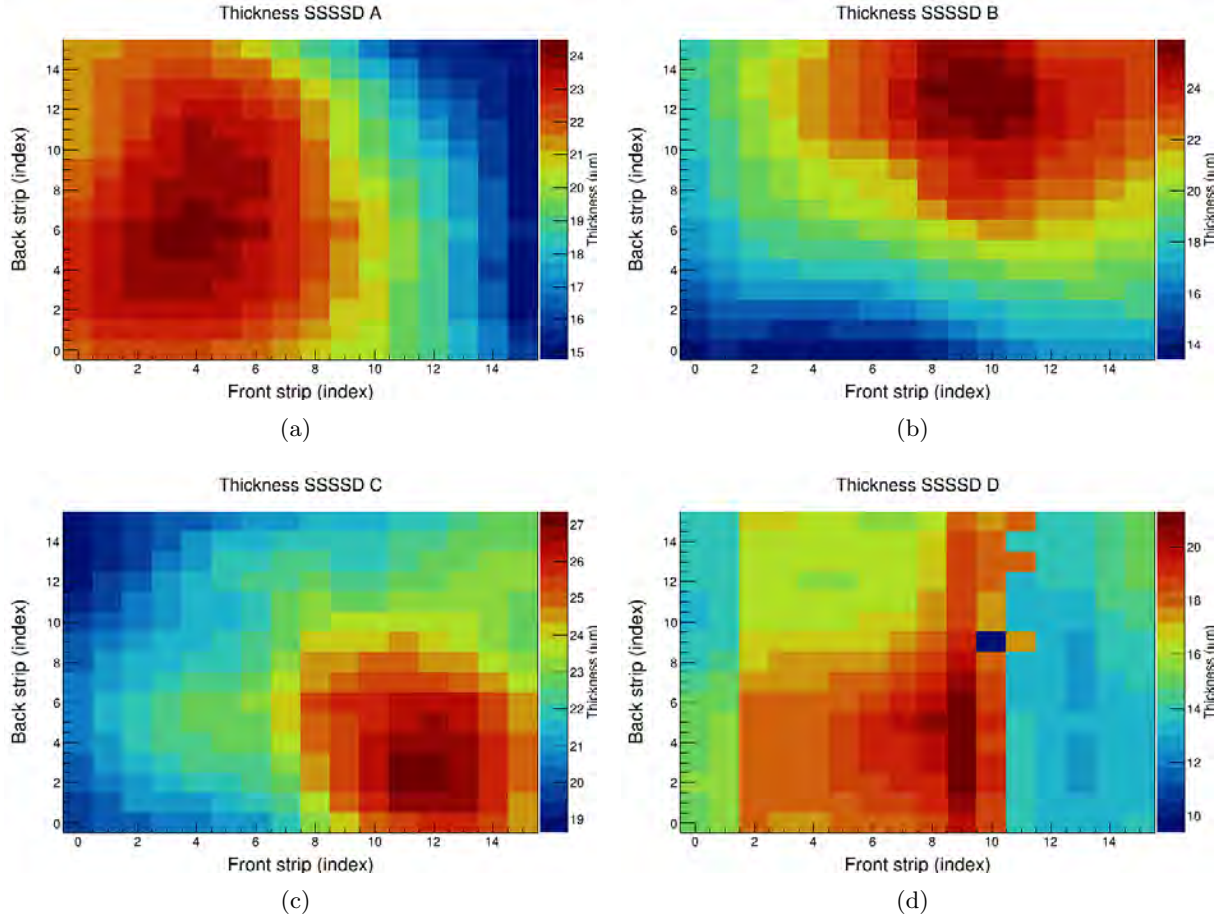
Figure 5.9: Nominal thickness (μm) of active material of the SSSSDs croseed by particles reaching DSSSD pixels, using the constant Stopping Power approach. The horizontal and vertical axis correspond to the indexes of the strips the define the pixels of this detector

5.5.2 Projected range approach

This second approach aims to account the increase in Stopping Power due to the loss of energy by the ^{10}Be in the medium. To do so, the Projected Range (Pr) Tables are used instead of the Stopping Power ones.

The Projected Range in function of the Energy was fitted by a second order polinomial in the range 10 to 30 MeV, obtaining the following parametrization:

$$Pr(E) = 0.02472E^2 + 1.198E + 1.206 \tag{5.10}$$

where E is the energy of the particle in MeV and Pr is in μm. This fit had a χ^2 of 6.8×10^{-4}. Having the Energy of the particle before the Si layer estimated by the approach followed in Subsection 5.4.3, the effective thickness of the layer would come as:

$$\mu = Pr(E_{before}) - Pr(E_{before} - E_{loss}) \tag{5.11}$$

by correcting this by with equation (5.8) the map of nominal thicknesses is obtained, under the same geometrical conditions of the maps in Subsection 5.5.1. These maps are shown in Figure 5.10
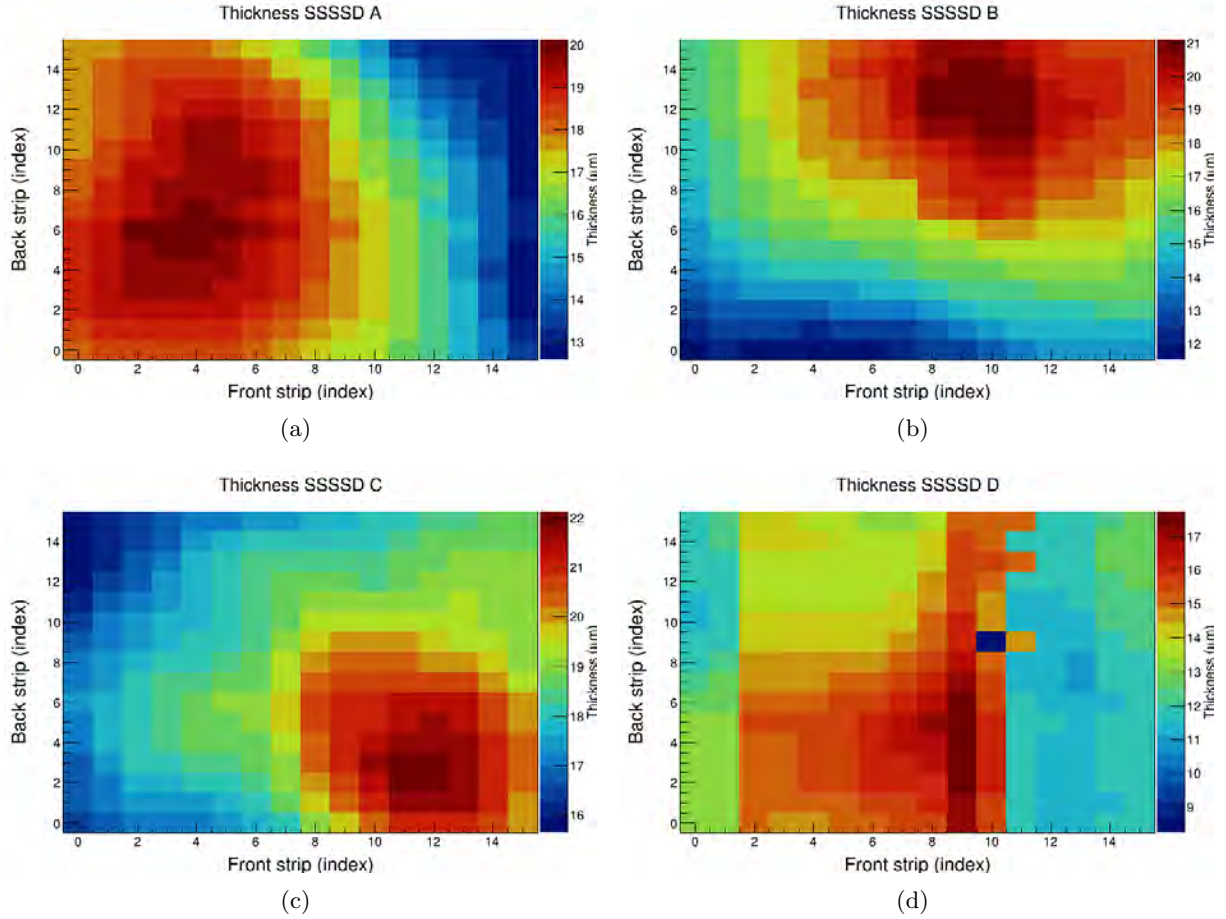
Figure 5.10: Nominal thickness (μm) of active material of the SSSSDs croseed by particles reaching DSSSD pixels, using the projected range approach. The horizontal and vertical axis correspond to the indexes of the strips the define the pixels of this detector

The two methods estimated values for the nominal thickness of the detector differing up to 35 % from the ones mentioned by the company that produces them [7]. The stopping range approach estimated higher thicknesses than the projected range approach. This is explainable through the fact that the Stopping Power increases with the reduction of the particle's energy. As the projected ranges approach considers this factor it is expected that it estimates a need of lower interaction length for the same energy deposited in a layer.

5.6 Corrections on Telescope 2D histograms

The impact of different thicknesses along a single strip of the SSSSD is notoriously seen when in Figure 5.11 where the spectrum of deposited energy in the SSSSD for particles reaching a given vertical strip of the second stage of the telescope is compared with the spectra from the pixels along that strip, defined by the Front and Back strip of the DSSSD.

As seen in Figure 5.11(b), each pixel's spectrum shows a single peak but there is a dispersion of the mean energy of the peak along the strip. The difference in thickness of the Si on the same strip results in different energy depositions for equal particles with roughly the same energy. The thickness maps in Figures 5.9 and 5.10 show the difference in nominal thickness for the two

dE C strip 12

(a)
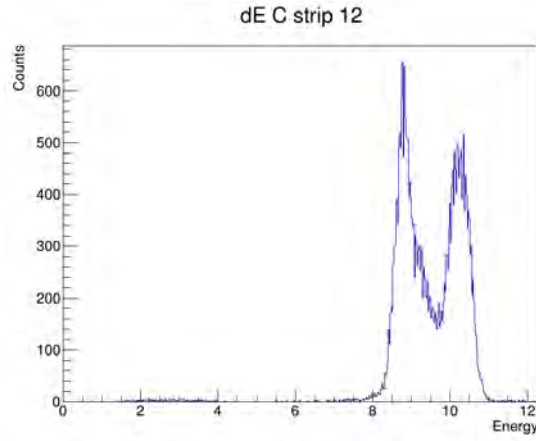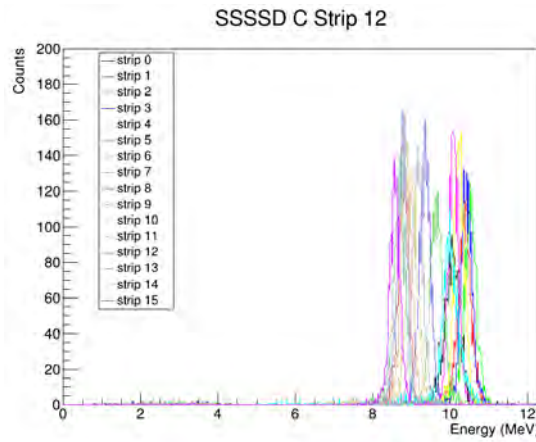
SSSSD C Strip 12

(b)

Figure 5.11: Energy measured in SSSSD C by particles emitted to strip #12 of DSSSD C Front in (a) and emitted to each of the pixels along that same vertical strip (b).The particles were products of the ^{10}Be+^{197}Au reaction with a beryllium beam at 27 MeV.

different approaches.

In order to correct thickness changes, it is possible to reverse each of the thickness determination approaches.

Considering the first approach, equation (5.9) can be reverted to obtain

$$\frac{E_{loss}}{\mu} = S(E_{before}) \tag{5.12}$$

Considering the Stopping Power to be constant for particles with the same energy while going through a very thin layer, the energy loss depends linearly on the thickness of the pixel and

$$\frac{E_{loss_j}}{\mu_j} = \frac{E_{loss_n}}{\mu_n} \tag{5.13}$$

where E_{loss_j} is the energy deposited in a layer with thickness μ_j. With this approach it is then

possible to estimate the energy that passed through μ_j would deposit in a layer of thickness μ_n with

$$E_{loss_n} = \frac{E_{loss_j}}{\mu_j} \times \mu_n \qquad (5.14)$$

In order to correct the dispersion seen in Figure 5.11 the factor $\frac{\mu_n}{\mu_j}$ was applied to the energy deposited in each event, where μ_n was the average effective thickness of the detector and μ_j the effective thickness that the particles reaching that pixel passed through in the SSSSD. Figure 5.12 shows the corrections performed in the strip seen in Figure 5.11.
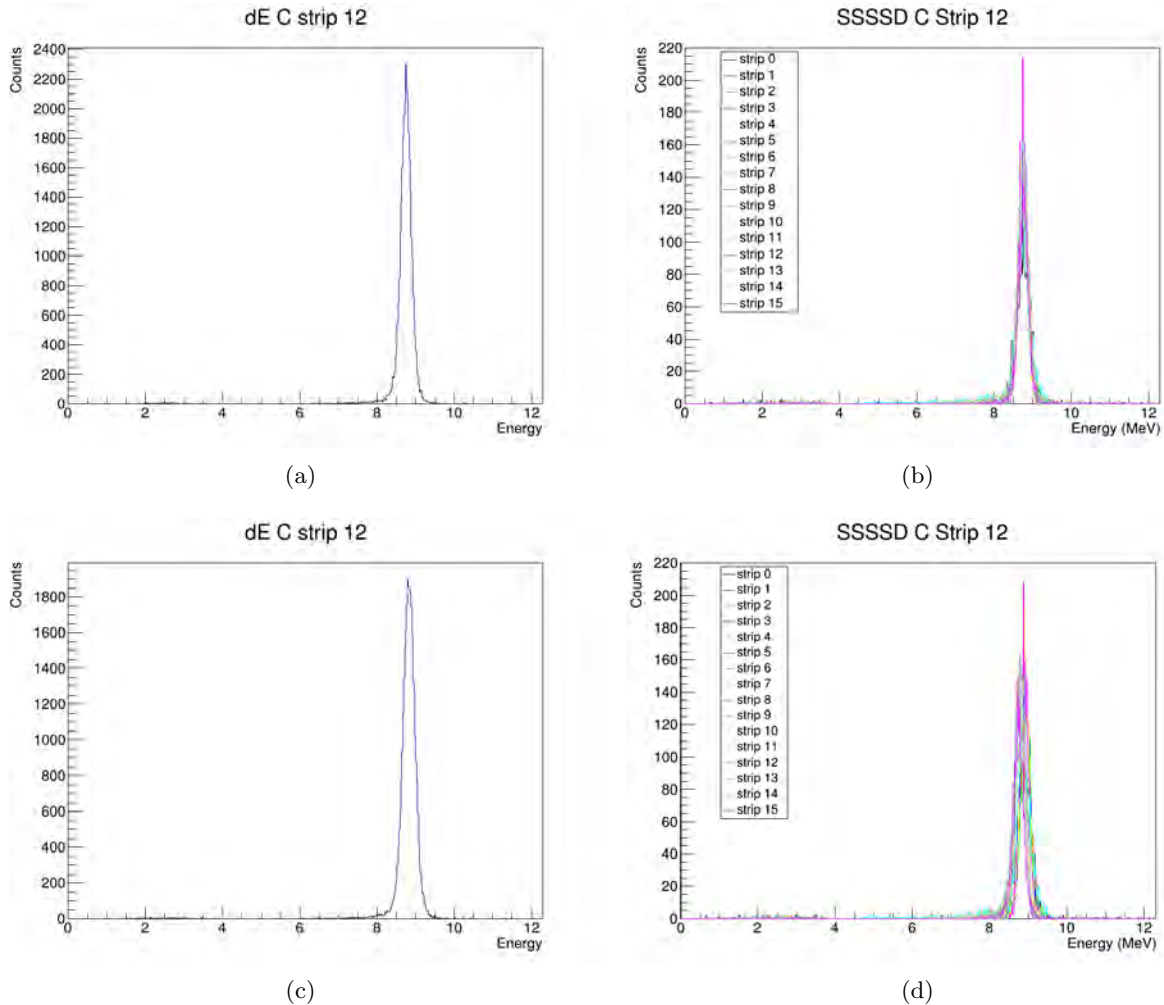

Figure 5.12: Measured energy in SSSSD C, corrected by the effective thickness, deposited by products of the ^{10}Be+^{197}Au reaction with a beryllium beam at 27 MeV. (a) for particles reaching strip #12 of DSSSD C Front, corrected by the thickness obtained with Stopping Power approach. (b) for particles reaching each pixel of strip #12 of DSSSD C Front, corrected by the thickness obtained with Stopping Power approach.(c) for particles reaching strip #12 of DSSSD C Front, corrected by the thickness obtained with projected range approach. (d) for particles reaching each pixel of strip #12 of DSSSD C Front, corrected by the thickness obtained with projected range approach.

Another possible approach would be to solve equation (5.11) for E_{loss}. However, this would depend on the parametrized curve used to estimate the projected range and also on the energy of the particle before crossing the active Si. Considering these requirements, in order to correct the energy deposited in the active layer as if all the particles crossed the same active thickness

Detector	SSSSD A			SSSSD B			SSSSD C		
Strip index	2	6	12	2	6	12	2	6	12
σ_E (keV)									
Before Correction	294	233	292	663	1163	953	309	239	642
Constant Stopping Power	147	130	177	179	173	140	167	156	141
Projected Ranges	149	132	178	188	200	167	168	157	160
Relative Difference (%)	1.34	1.51	0.56	4.79	13.5	16.17	0.6	0.64	11.88

Table 5.5: Comparison between the standard deviation of t

uses (**??**). The corrected energy (E^*_{loss}) is comes given by

$$E^*_{loss_j} = E_{loss_j} \times \frac{\mu_{avg}}{\mu_j} \tag{5.15}$$

In Table 5.13 is shown the comparison between the standard deviation (σ_E) of the gaussian function fitted to the elastic peak measured in individual strips before and after each correction. The correction method does not consider the increase in Stopping power with the decrease of energy while crossing the active material of the detector. Hence, the second approach will expectedly perform worse than the constant Stopping Power approach, for corrections done in as described. The comparison was made by taking the relative difference between the σ_E obtained from corrections with each approach and was found to be greater for strips with higher changes in thickness.

5.7 Impact of thickness characterization experimental analysis

As discussed previously in Subsection 4.2.1, a common way to represent the data measured in a telescope is the Energy deposited in the ΔE as a function of the sum of the energy measured in the whole telescope.

Without the correction for the effective thickness of a pixel, there will be a dispersion of the data along the vertical axis. This is due to the fact that particles expected to deposit the same energy on the thin layer of the telescope will deposited more (in case the pixel is effectively thicker than the average) or less (in case the pixel is thinner than the average). The remaining energy will then be deposited in the thicker layer, which accounts for the same sum energy on the horizontal axis. As the energy measured in the sum axis correspond to the actual energy deposited in the active layers, the correction must be applied only to the vertical axis, which brings each point to E^*_{loss} as a function of $E_{loss} + E_{thick}$. In Figure 5.13 it is seen the difference between these representations with and without corrections, considering the thicknesses obtained with the Stopping Power approach.

After the correction is observed a clear improvement of resolution, as seen in Figure 5.14. It is possible to distinguish ^{10}Be nuclei coming from quasi-elastic reactions and ^{9}Be from ^{9}Be $+ n$ breakup. In addition, it is also possible to observe the signatures of ^{6}He and ^{4}He nuclei from another possible breakup channel.
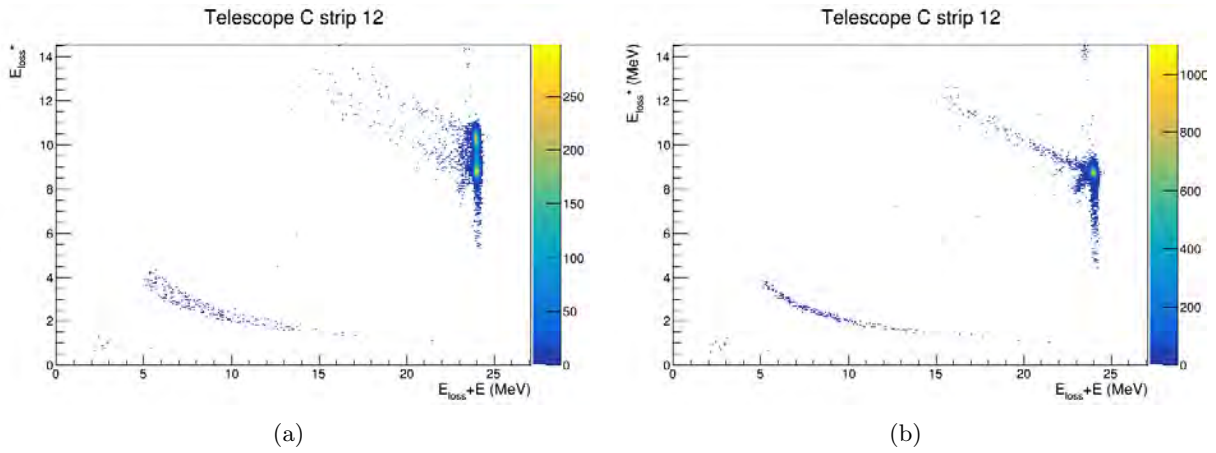
(a)   (b)

Figure 5.13: Telescope histograms of particles reaching strip #12 of DSSSD C from ^{10}Be+^{197}Au reaction with berylium beam at 27 MeV, before (a) and after (b) the correction of the ΔE value in the vertical axis.
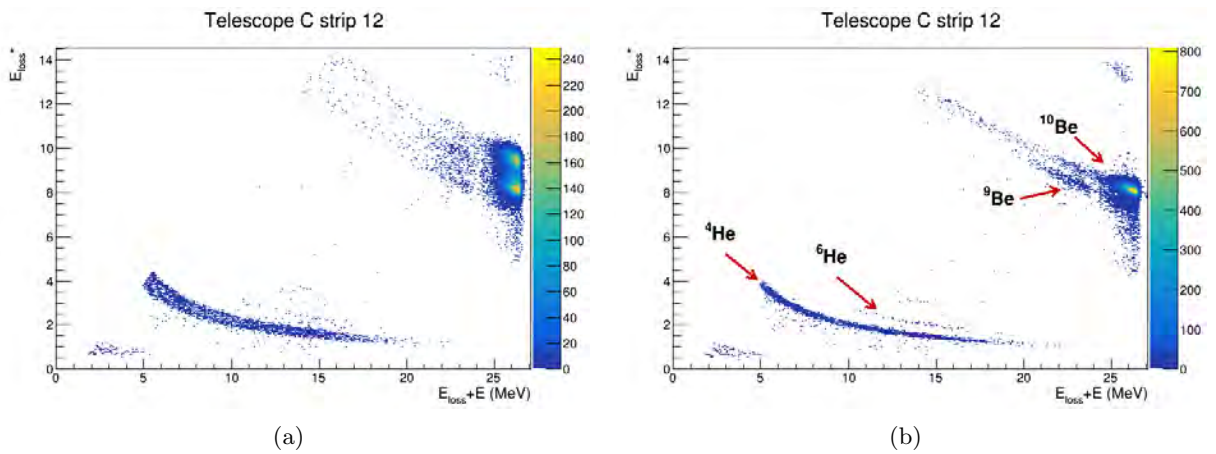

(a)   (b)

Figure 5.14: Telescope histograms of particles reaching strip #12 of DSSSD C from ^{10}Be+^{120}Sn reaction with berylium beam at 31 MeV, before (a) and after (b) the correction of the ΔE value in the vertical axis.

Chapter 6

Conclusions

In the framework of the present work, it was accurately determined the thickness of the ΔE SSSSDs detectors used in the measurement of the reaction ^{10}Be$+^{120}$Sn, performed at INFN-LNS laboratory. The main conclusions and results are summarized as follow:

1. The study and understanding of the experiment's geometry allowed for better selection of events when dealing with conditions over the strips of both stages of the Telescopes.

2. The assessed parameters on the optimization of the positioning and orientation of the detectors were crucial for a fine energy calibration of the SSSSDs. This study also motivated a deeper study of the solid angle that allowed its accurate estimation under different orientations of the detector.

3. The standard deviation σ_{diff} of the DSSSDs is used as a condition to validate the analysed events. For an event to be valid it must have fulfill $E_{Back} = E_{Front} \pm 3\sigma_E$ since the charge generated by a particle on the front side of the detector has to be equal to that generated in the back side, we have considered $E_{Back} = E_{Front} \pm 3\sigma_E$. The performed correction reduced σ_E from 590 keV down to 15.83 keV in the most severe correction. Other corrections lowered this value to about its half.

4. The estimation of the energy deposited in the active region of the SSSSDs by the particles considered for its energy calibration, resulted in corrections of up to 8%. The consideration of the entrance angle in the detector modified the energy of the α-particles coming from ^{148}Gd went down from 3.183 MeV to 2.928 MeV. The correction on the energies of particles coming from the scattering reactions was most impacted by the struggling in the material. Thus, a $\sim$8% correction was applied for all strips.

5. The calculated thickness es of the active layer of the SSSSDs showed deviations from the 20 μm nominal thickness of up to 35%.

6. The correction of histograms with E_{loss} as a function of the total energy measured in the telescope was found to benefit when the thicknesses considered were obtained through the constant stopping power approach, when compared to the other approach analysed. Even though it is a rougher method for the estimation of the thickness, the correction of ΔE follows a similar approach in order to be independent of the particle being detected. The σ_E measured in a single strip was found to be up to 17% lower for the constant stopping

power approach when compared with the projected ranges approach. This difference was found to be higher for strips with lower thickness homogeneity.

7. The applied corrections enhanced the particle's characteristic curves in spectra from experimental runs which allows the identification of particles that were previously indistinguishable.

For future experiments, it is also strongly recommended the use of scattering reactions for the calibration of the second stage of the Telescopes, if energies higher than 5 MeV are to be measured in this stage. This would allow for a better energy calibration in the relevant energy being measured, possibly reducing the need for a gain match.

The work presented will allow to proceed with the analysis of data from the BESN experiment. The detailed thickness characterization and energy corrections will allow precise measurements of the angular and energy distribution of the different fragments of the reactions taking place.

Bibliography

[1] H. Becquerel, "The lund/lbnl nuclear data search." `https://gallica.bnf.fr/ark:/12148/bpt6k30780/f503.item#`. Accessed: 24-02-2021.

[2] P. Molinié and S. Boudia, "Mastering picocoulombs in the 1890s: The curies' quartz–electrometer instrumentation, and how it shaped early radioactivity history," *Journal of Electrostatics*, vol. 67, no. 2, pp. 524–530, 2009. 11th International Conference on Electrostatics.

[3] E. R. M. B.Sc., "Viii. uranium radiation and the electrical conduction produced by it," *The London, Edinburgh, and Dublin Philosophical Magazine and Journal of Science*, vol. 47, no. 284, pp. 109–163, 1899.

[4] W. Crookes, "The emanations of radium," *Proceedings of the Royal Society of London*, vol. 71, pp. 405–408, 1902.

[5] K. G. McKay, "A. germanium counter," *Physical Review (Series I) vol. 76 iss. 10*, vol. 76, nov 1949.

[6] M. Turala, "Silicon tracking detectors—historical overview," *Nuclear Instruments and Methods in Physics Research Section A: Accelerators, Spectrometers, Detectors and Associated Equipment*, vol. 541, no. 1, pp. 1–14, 2005. Development and Application of Semiconductor Tracking Detectors.

[7] "Micron semiconductor ltd.." `http://www.micronsemiconductor.co.uk/product/w1/`. Accessed: 10-02-2021.

[8] G. F. Knoll, *Radiation detection and measurement / Glenn F. Knoll.* Wiley New York, 2nd ed. ed., 1989.

[9] K. S. Krane, D. Halliday, *et al.* 1987.

[10] C. Iliadis, *Nuclear Physics of Stars.* 02 2007.

[11] M. Leone, N. Robotti, and G. Verna, "'rutherford's experiment' on alpha particles scattering: the experiment that never was," *Physics Education*, vol. 53, p. 035003, feb 2018.

[12] H. Geiger and E. Marsden, "On a diffuse reflection of the -particles," *Proceedings of the Royal Society of London. Series A, Containing Papers of a Mathematical and Physical Character*, vol. 82, no. 557, pp. 495–500, 1909.

[13] H. Geiger and E. Rutherford, "On the scattering of the α-particles by matter," *Proceedings of the Royal Society of London. Series A, Containing Papers of a Mathematical and Physical Character*, vol. 81, no. 546, pp. 174–177, 1908.

[14] N. J. Zaluzec, "Analytical formulae for calculation of x-ray detector solid angles in the scanning and scanning/transmission analytical electron microscope," *Microscopy and Microanalysis*, vol. 20, no. 4, p. 1318–1326, 2014.

[15] W. S. Boyle and G. E. Smith, "Charge coupled semiconductor devices," *The Bell System Technical Journal*, vol. 49, no. 4, pp. 587–593, 1970.

[16] S. Luryi, A. Kastalsky, and J. Bean, "New infrared detector on a silicon chip," *IEEE Transactions on Electron Devices*, vol. 31, no. 9, pp. 1135–1139, 1984.

[17] K. J, "Fabrication of low-noise silicon radiation detectors by the planar process," *Nucl. Instrum. Methods; (Netherlands)*, vol. 169:3, Mar 1980.

[18] P. Laube, "Semiconductor technology from a to z."

[19] Z. He, "Review of the shockley–ramo theorem and its application in semiconductor gamma-ray detectors," *Nuclear Instruments and Methods in Physics Research Section A: Accelerators, Spectrometers, Detectors and Associated Equipment*, vol. 463, no. 1, pp. 250–267, 2001.

[20] G. Parker, *Introductory Semiconductor Device Physics*. CRC Press, 2004.

[21] W. R. Leo and D. G. Haase, "Techniques for nuclear and particle physics experiments," *American Journal of Physics*, vol. 58, no. 12, pp. 1216–1217, 1990.

[22] Q. Liu *et al.*, "Investigation of the thickness non-uniformity of the very thin silicon-strip detectors," *Nuclear Instruments and Methods in Physics Research Section A: Accelerators, Spectrometers, Detectors and Associated Equipment*, vol. 897, pp. 100–105, 2018.

[23] P. Azzurri, "The CMS silicon strip tracker," *Journal of Physics: Conference Series*, vol. 41, pp. 127–134, may 2006.

[24] G. Marquínez-Durán, L. Acosta, R. Berjillos, J. Dueñas, J. Labrador, K. Rusek, A. Sánchez-Benítez, and I. Martel, "Gloria: A compact detector system for studying heavy ion reactions using radioactive beams," *Nuclear Instruments and Methods in Physics Research Section A: Accelerators, Spectrometers, Detectors and Associated Equipment*, vol. 755, pp. 69–77, 2014.

[25] M. Mazzocco, N. Keeley, A. Boiano, C. Boiano, M. L. Commara, A. Lagni, C. Manea, C. Parascandolo, D. Pierroutsakou, C. Signorini, E. Strano, D. Torresi, H. Yamaguchi, D. Kahl, L. Acosta, D. Meo, J. P. Fernandez-Garcia, T. Glodariu, J. Grebosz, A. Guglielmetti, Y. Hirayama, N. Imai, H. Ishiyama, N. Iwasa, S. C. Jeong, H. M. Jia, Y. H. Kim, S. Kimura, S. Kubono, G. L. Rana, C. J. Lin, P. Lotti, G. Marquínez-Duran, I. Martel, H. Miyatake, M. Mukai, T. Nakao, M. Nicoletto, A. Pakou, K. Rusek, Y. Sakaguchi, A. M. Sánchez-Benítez, T. Sava, O. Sgouros, V. Soukeras, F. Soramel, E. Stiliaris, L. Stroe, T. Teranishi, N. Toniolo, Y. Wakabayashi, Y. X. Watanabe, L. Yang, Y. Y. Yang, and

H. Q. Zhang, "Direct processes for the systems 7be,8b 208pb at coulomb barrier energies," *Journal of Physics: Conference Series*, vol. 1643, p. 012096, dec 2020.

[26] R. Greenwood, "The neutron binding energies of 10be and 24na determined from neutron capture gamma-ray energy measurements," *Physics Letters*, vol. 23, no. 8, pp. 482–484, 1966.

[27] D. Dell'Aquila, I. Lombardo, L. Acosta, R. Andolina, L. Auditore, G. Cardella, M. B. Chatterjiee, E. De Filippo, L. Francalanza, B. Gnoffo, G. Lanzalone, A. Pagano, E. V. Pagano, M. Papa, S. Pirrone, G. Politi, F. Porto, L. Quattrocchi, F. Rizzo, E. Rosato, P. Russotto, A. Trifirò, M. Trimarchi, G. Verde, and M. Vigilante, "New experimental investigation of the structure of ^{10}Be and ^{16}C by means of intermediate-energy sequential breakup," *Phys. Rev. C*, vol. 93, p. 024611, Feb 2016.

[28] R. Greenwood, "The neutron binding energies of 10be and 24na determined from neutron capture gamma-ray energy measurements," *Physics Letters*, vol. 23, no. 8, pp. 482–484, 1966.

[29] M. A. G. Alvarez, M. Rodríguez-Gallardo, L. R. Gasques, L. C. Chamon, J. R. B. Oliveira, V. Scarduelli, A. S. Freitas, E. S. Rossi, V. A. B. Zagatto, J. Rangel, J. Lubian, and I. Padron, "Elastic scattering, inelastic excitation, and $1n$ pick-up transfer cross sections for ^{10}B + ^{120}Sn at energies near the coulomb barrier," *Phys. Rev. C*, vol. 98, p. 024621, Aug 2018.

[30] L. R. Gasques, M. A. G. Alvarez, A. Arazi, B. V. Carlson, L. C. Chamon, J. P. Fernández-García, A. Lépine-Szily, J. Lubian, J. Rangel, M. Rodríguez-Gallardo, V. Scarduelli, and V. A. B. Zagatto, "Understanding the mechanisms of nuclear collisions: A complete study of the ^{10}B +^{120} Sn reaction," *Phys. Rev. C*, vol. 103, p. 034616, Mar 2021.

[31] J. J. Kolata, E. F. Aguilera, F. D. Becchetti, Y. Chen, P. A. DeYoung, H. García-Martínez, J. D. Hinnefeld, J. H. Lupton, E. Martinez-Quiroz, and G. Peaslee, "Elastic scattering of ^{10}Be on ^{208}Pb near the coulomb barrier," *Phys. Rev. C*, vol. 69, p. 047601, Apr 2004.

[32] A. Arazi, J. Casal, M. Rodríguez-Gallardo, J. M. Arias, R. Lichtenthäler Filho, D. Abriola, O. A. Capurro, M. A. Cardona, P. F. F. Carnelli, E. de Barbará, J. Fernández Niello, J. M. Figueira, L. Fimiani, D. Hojman, G. V. Martí, D. Martínez Heimman, and A. J. Pacheco, "^{9}Be +^{120} Sn scattering at near-barrier energies within a four-body model," *Phys. Rev. C*, vol. 97, p. 044609, Apr 2018.

[33] P. Figuera, E. Maugeri, R. Buompane, L. Cosentino, A. Di Leva, A. Di Pietro, M. Fisichella, L. Gialanella, S. Heinitz, N. Kivel, M. Lattuada, C. Marchetta, S. Marletta, D. Mascali, A. Massara, D. Schumann, and F. Tudisco, "Development of an intense 10be radioactive beam in 'off-line mode' at the catania tandem accelerator," *Nuclear Instruments and Methods in Physics Research Section A: Accelerators, Spectrometers, Detectors and Associated Equipment*, vol. 972, p. 164120, 2020.

[34] R. de Diego, J. M. Arias, J. A. Lay, and A. M. Moro, "Continuum-discretized coupled-channels calculations with core excitation," *Phys. Rev. C*, vol. 89, p. 064609, Jun 2014.

[35] D. Rifuggiato, L. Calabretta, L. Celona, F. Chines, L. Cosentino, G. Cuttone, P. Finocchiaro, A. Pappalardo, M. Re, and A. Rovelli, "Radioactive ion beam facilities at infn lns," *Journal of Physics: Conference Series*, vol. 267, 01 2011.

[36] Danilo Rifuggiato, "Status of the infn-lns accelerator facility," *ECOS Facility Meeting*, 2013.

[37] S. Heinitz, D. Kiselev, N. Kivel, and D. Schumann, "Separation of weighable amounts of 10be from proton irradiated graphite," *Applied Radiation and Isotopes*, vol. 130, pp. 260–263, 2017.

[38] D. Schumann, J. Neuhausen, S. Horn, P. W. Kubik, and I. Günther-Leopold, "Radiochemical separation and analytical determination of 10be from proton-irradiated graphite targets," *Radiochimica Acta*, vol. 96, no. 1, pp. 31–34, 2008.

[39] "The ct-2000 scattering chamber." `https://www.lns.infn.it/en/equipment/scattering-rooms/ct2000.html`. Accessed: 22-02-2021.

[40] Mesytec, "Mpr-16 datasheet." `http://www.mesytec.eu/products/datasheets/MPR-16.pdf`. Accessed: 23-03-2022.

[41] Mesytec, "Mscf-16 f datasheet." `http://www.mesytec.com/products/datasheets/MSCF16-F-V.pdf`. Accessed: 23-03-2022.

[42] CAEN, "V785 datasheet." `https://www.caen.it/products/v785/`. Accessed: 23-03-2022.

[43] CAEN, "V785 datasheet." https://www.caen.it/products/n454/. Accessed: 23-03-2022.

[44] CAEN, "V977." https://www.caen.it/products/v977/. Accessed: 23-03-2022.

[45] L. E. S.Y.F. Chu and R. Firestone, "The lund/lbnl nuclear data search." `http://nucleardata.nuclear.lu.se/toi/`. Accessed: 10-02-2021.

[46] R. Brun and F. Rademakers, "Root - an objectoriented data analysis framework," *Nucl. Instrum.Meth.A38981*, 1997.

[47] J. F. Ziegler, M. D. Ziegler, and J. P. Biersack, "SRIM - The stopping and range of ions in matter (2010)," *Nuclear Instruments and Methods in Physics Research B*, vol. 268, pp. 1818–1823, June 2010.